Geochemistry Geophysics Geosystems G3
AN ELECTRONIC JOURNAL OF THE EARTH SCIENCES
Published by AGU and the Geochemical Society

Article
Volume 7, Number 11
22 November 2006
Q11018, doi:10.1029/2006GC001409
ISSN: 1525-2027

Conduit diameter and buoyant rising speed of mantle plumes: Implications for the motion of hot spots and shape of plume conduits

B. Steinberger
Center for Geodynamics, NGU, Leiv Eirikssons Vei 39, N-7491 Trondheim, Norway (bernhard.steinberger@ngu.no)

M. Antretter
Department of Earth and Environmental Sciences, University of Munich, Theresienstr. 41, D-80333 Munich, Germany

Now at Deutsches Patent- und Markenamt, D-80297 Munich, Germany (maria.antretter@dpma.de)

[1] Mantle plumes are expected to be affected by large-scale flow in the Earth's mantle related to plate motions, subducted slabs, and possibly large-scale upwellings. Motion of plume conduits will depend on both large-scale flow and buoyant rising speed of the conduit through the mantle. Here we present a model of depth-dependent plume conduit temperature, viscosity, radius, and buoyant rising speed and use it to compute plume and hot spot motion. Results support a temperature anomaly of about 500 K at the plume base. In this case, sublithospheric temperature anomaly is about 150 K for the Iceland plume; transition zone anomaly is between 150 and 200 K for Iceland, about 250 K for Samoa, and about 300 K for Hawaii. Thermal plume radii are about 100 km in the upper mantle, increasing to about 200 km in the lower mantle. Beneath the lithosphere, viscosity in the vicinity of plumes is substantially reduced compared to the underlying mantle, and fast-moving plates deflect plumes by 200 km or less, corresponding to a plume conduit buoyant rise time of about 3 Myr between 400 and 100 km depth, where most of the shear flow due to plate motions occurs. During 100 Myr, plume conduits rise buoyantly from about 1500–2000 km depth. In many cases, computed hot spot motion agrees with previous computations: south-southeastward motion of the Hawaiian hot spot during the past 100 Myr, Louisville hot spot motion in a similar direction but at slower speed during the past 50 Myr, and westward motion of the Easter hot spot relative to Hawaii and Louisville. However, the previously computed substantial southward motion of the Kerguelen hot spot is not confirmed. If plume sources in the lowermost mantle are assumed to move with large-scale flow, they are predicted to be displaced toward the two large-scale upwellings beneath Africa and the Pacific relative to hot spot surface locations. For fixed sources, predicted tilts of the lower part of conduits tend to be opposite to that.

Components: 12,802 words, 16 figures, 1 table.

Keywords: plume.

Index Terms: 0560 Computational Geophysics: Numerical solutions (4255); 8137 Tectonophysics: Hotspots, large igneous provinces, and flood basalt volcanism; 8121 Tectonophysics: Dynamics: convection currents, and mantle plumes.

Received 3 July 2006; **Revised** 25 August 2006; **Accepted** 11 September 2006; **Published** 22 November 2006.

Steinberger, B., and M. Antretter (2006), Conduit diameter and buoyant rising speed of mantle plumes: Implications for the motion of hot spots and shape of plume conduits, *Geochem. Geophys. Geosyst.*, *7*, Q11018, doi:10.1029/2006GC001409.

1. Introduction

[2] Hot spots are locations of intraplate volcanism, such as Hawaii, or especially vigorous volcanism along plate boundaries, such as Iceland, and are often used as reference points for absolute plate motions [*Morgan*, 1972]. A common reference frame is needed in order to understand the dynamical links between plate motions and processes in the deeper mantle. Furthermore, in cases where relative plate motions are otherwise not well constrained (e.g., between the Pacific and African hemisphere prior to about 47 Ma) a suitable "absolute" reference frame can also help to improve relative plate motion models [*Steinberger et al.*, 2004].

[3] Hot spots are often considered to be fixed relative to each other, and with respect to the underlying mantle. However, the arguably most widely accepted explanation for their origin is that they are the surface expression of deep, narrow, mantle upwellings, so-called plumes [*Morgan*, 1972], and if plume conduits are embedded in a convecting mantle, they should also move. Moreover, there is observational evidence for such motion [*Tarduno et al.*, 2003]. A model of hot spot motion is therefore necessary for devising a suitable reference frame. The model should be able to explain observations where they exist and make predictions where they do not. Ultimately whether or not a model of hot spot motion, based on the assumption of deep mantle plumes, is successful in explaining observations, and whether or not predictions of the model can be confirmed by future observations, will help to assess whether the concept of deep mantle plumes as the origin of hot spots is viable, or whether alternative explanations should be favored.

[4] A model of plume conduit and hot spot motion has been developed [*Steinberger and O'Connell*, 1998] and applied to a hot spots globally [*Steinberger*, 2000]. This model is simplified in that only large-scale mantle flow is computed dynamically. In a second step, the motion of each part of the plume conduit is computed as vector sum of (1) large-scale mantle flow and (2) buoyant rising speed, which is assumed to depend on depth in the mantle. The plume conduit is assumed to be initially vertical at a time equal to its assumed age. This approach has the advantage of being computationally very effective. It thus allows a large number of model runs within short time, thus allowing to optimize the fit to observations by varying a number of model parameters in a certain range that is compatible with observations [*O'Neill et al.*, 2005] and to test the robustness of model predictions.

[5] Results of the simplified model depend on (1) the large-scale mantle flow model and (2) assumed buoyant rising speed. Optimizing the former to fit constraints from mineral physics and surface observations is topic of another paper [*Steinberger and Calderwood*, 2006]; here we focus on the latter. In previous work [e.g. *Steinberger and O'Connell*, 1998, 2000; *Steinberger*, 2000; *Antretter et al.*, 2002, 2004; *Tarduno et al.*, 2003; *Steinberger et al.*, 2004; *O'Neill et al.*, 2003, 2005] a range of assumptions on buoyant rising speed was already explored. Computed hot spot motion tends to represent flow at some depth in the lower mantle. Here, our motivation is to use a buoyant rising speed that is as realistic as possible, taking into account recent experimental, theoretical, observational and numerical results, in order to either reconfirm or modify our previous modeling predictions.

[6] Computation of plume buoyant rising speed is done in four steps, which are computed one after the other: (1) plume and ambient mantle temperature versus depth; (2) plume and ambient mantle viscosity versus depth; (3) plume radius versus depth; and (4) plume rising speed versus depth. A second motivation of this paper is therefore to show that our model is consistent with a number of observations along these steps, and to provide a framework of how future observations can be used to test our model.

[7] In the next section we give the necessary background on observations, theory, experiments and modeling regarding these four steps, and their relation to each other. We discuss work pertaining to the questions to which areas of intraplate vol-

canism we wish to apply our model of deep plume origin to, where the plumes are located now, how old and how strong (in terms of anomalous mass flux) they are, whether a plume source in the lowermost mantle is moving or "anchored," and what observations our results on hot spot motions and plume conduit shape can be compared to. In section 3 we describe our computation of large-scale mantle flow and buoyant plume rising speed, concentrating on new methodology. In section 4, new findings pertaining to the above listed four steps, and predicted conduit shape and hot spot motion are presented and compared to our previous results or assumptions. In section 5 we discuss results in the context of observations and other models. The last section includes perspectives for future work.

2. Background

2.1. Temperatures in Plumes and Ambient Mantle

[8] At shallow depth, temperature anomalies in plumes relative to the ambient mantle can be estimated from the extra crustal thickness at hot spots in combination with models of pressure-release partial melting. *Schubert et al.* [2001] generally estimate 200–300 K. *Ruedas et al.* [2004] obtain 150–200 K for the Iceland plume, confirming earlier findings. *Putirka* [2005] infers from olivine phenocrysts mantle potential temperatures at Hawaii 213–235 K and Iceland 162–184 K hotter than ambient mid-ocean ridges, respectively.

[9] For the transition zone, temperature anomalies can be estimated from the Clapeyron slopes of the two phase boundaries at about 400 and 660 km depth and the distance between the phase boundaries ("transition zone thickness") which is determined seismologically. *Shen et al.* [1998, 2002] obtain ≈150 K for Iceland, *Niu et al.* [2002] find 170–220 K for Tahiti, and *Li et al.* [2000] find ≈300 K for Hawaii.

[10] Temperature anomalies can also be estimated from seismic tomography and scaling seismic velocity to temperature anomalies. For Iceland, the tomography model of *Hung et al.* [2004], which was obtained with a finite-frequency approach, yields somewhat larger temperature anomalies than the above numbers, and even larger anomalies follow for a narrower plume [*Allen and Tromp*, 2005]. However, seismic velocity may also be reduced due to partial melting. A number of other plumes are resolved in the mid-mantle by *Montelli et al.* [2004]. They typically find p-wave anomalies of less than 1%, corresponding to s-wave anomalies of about 1%.

[11] These observation-based estimates can be compared to results from numerical models. *Albers and Christensen* [1996] compute temperature anomalies as a function of depth for different plume strength (expressed in terms of anomalous mass flux) and different starting temperature anomalies at their base in the lowermost mantle. They find that results approximately match observations, if plumes start with an excess temperature of about 500 K. Strong plumes then arrive beneath the lithosphere with a temperature anomaly of about 250–300 K, whereas weak plumes with a buoyancy flux of about 500 kg/s have only 150 K or less anomaly in the upper mantle, due to thermal diffusion. Even weaker plumes would be diffused away even before reaching the lithosphere, and plumes with smaller anomalous mass fluxes perhaps rise from shallower depth. 500 K excess temperature in the lowermost mantle is much less than the expected temperature difference in the thermal boundary layer between mantle and core [*Boehler*, 1996] and therefore may be an indication for plumes rising from the top of a compositionally distinct layer at the base of the mantle [*Farnetani*, 1997].

[12] *Albers and Christensen* [1996] present in their Figure 4 temperature anomaly as a function of nondimensional heat flux and dissipation number. In order to extract temperature anomalies as a function of depth for different anomalous mass fluxes, heat capacity C_p, and averages of density ρ, thermal expansivity α, thermal diffusivity κ and gravity γ between the base of the conduit and height h above its base are needed. *Stacey* [1992] and *Schubert et al.* [2001] consider C_p = 1250 J kg^{-1}K^{-1} appropriate for heat capacity. Experimental data show that κ increases with depth. A value $\kappa_0 = 0.75\ 10^{-6}$ m^2/s at shallow depth and a factor ≈2 increase through the mantle appears roughly consistent with a number of considerations [*Schubert et al.*, 2001; *Xu et al.*, 2004]. A strong decrease of thermal expansivity $\alpha(z)$ with depth is inferred from experiments [*Chopelas and Boehler*, 1989].

[13] An adiabatic temperature profile can be derived jointly with $\alpha(z)$; the profile of *Steinberger and Calderwood* [2006] is very similar to the reference mantle adiabat of *Schubert et al.*

[2001]. The temperature estimate above the bottom thermal boundary layer is about 2500 K, compared to 4000 ± 600 K at the core-mantle boundary (CMB) [*Boehler*, 1996].

2.2. Viscosities in the Ambient Mantle and Plumes

[14] Strain rates $\dot{\epsilon}$ and stresses σ in the mantle are frequently assumed to be related through

$$\dot{\epsilon} \sim \sigma^n \exp\left(-\frac{H}{RT}\right) \quad (1)$$

whereby H is activation enthalpy, R is the universal gas constant, T is temperature. The relation is either linear ($n = 1$, for diffusion creep) or nonlinear (for dislocation creep; $n \approx 3.5$). Both creep mechanisms may contribute to the flow, but it is often thought that dislocation creep is the dominant mechanism in the upper mantle [*Ranalli*, 1995; *Schubert et al.*, 2001], whereas diffusion creep is dominant in the lower mantle [*Karato et al.*, 1995]. A nonlinear relationship can be linearized yielding an effective viscosity

$$\eta \sim \exp\left(\frac{rH}{RT}\right) \quad (2)$$

with $r = 1/n$ for the assumption of constant strain rate, $r = 2/(n + 1)$ for constant dissipation rate and $r = 1$ for constant stress. *Christensen* [1983] found $r = 0.3–0.5$ appropriate for $n = 3$; with an activation enthalpy reduced in that way, the properties of non-Newtonian flow can be closely mimicked by Newtonian flow in 2-D numerical experiments.

[15] Activation enthalpy has been directly estimated by *Ranalli* [1995] and *Calderwood* [1999]. In the upper mantle, both profiles are very similar. A relation

$$H = gRT_m \quad (3)$$

with melting temperature T_m had been proposed [*Weertman and Weertman*, 1975]. Melting temperature profiles have been determined for lower mantle constituents $MgSiO_3$ perovskite [*Wang*, 1999] and MgO [*Zerr and Boehler*, 1994]; these profiles are similar and considered appropriate for the lower mantle by *Yamazaki and Karato* [2001] who also determined $g \approx 14$ for $MgSiO_3$ and 10 for MgO.

[16] Radial viscosity profiles for the ambient mantle were determined by *Steinberger and Calderwood* [2006]. Relative viscosity variations with depth in mantle layers (upper mantle, transition zone, lower mantle) were inferred from mineral physics considerations as outlined above. Absolute viscosity values were chosen such as to optimize the fit of model predictions to observational constraints (geoid, heat flux profile, Haskell viscosity average). They found no clear preference for either a viscosity low in the asthenosphere or transition zone. The profile with lowest viscosity in the asthenosphere is similar to the one used by *Steinberger and O'Connell* [1998] to model hot spot motion.

[17] Viscosity in the asthenosphere in the vicinity of plumes might be considerably lower than in these profiles, though, due to hot material flowing out of the plume and the possibility of partial melting. Presence of melt may lead to a stronger viscosity contrast than determined from the temperature contrast between plume and surrounding mantle. *Schubert and Hey* [1986] determined asthenospheric viscosity between 10^{17} and 10^{18} Pas beneath the propagating tip of the Galapagos rift system in the vicinity of the Galapagos plume. *Albers and Christensen* [2001] found similar asthenospheric viscosities for those models of the Iceland plume for which channeling of plume material to the ridge occurs, and which are hence capable of explaining the V-shaped patterns along the ridge south of Iceland. The ratio of viscosity along the centerline of a plume conduit η_{in} to ambient mantle viscosity η_{out} is inferred from equation (2) as

$$\eta_{in}/\eta_{out} = \exp\left(\frac{-rH\Delta T_0}{RT_0(T_0 + \Delta T_0)}\right) \quad (4)$$

whereby T_0 is the temperature in the ambient mantle and ΔT_0 is the centerline plume temperature anomaly.

2.3. Plume Radius

[18] From the tomography model of *Hung et al.* [2004], a radius somewhat larger than 100 km is inferred for the Iceland plume in the upper mantle, and no strong variations of radius with depth. *Allen and Tromp* [2005] infer from the seismic velocity structure a conduit radius most likely between 75 and 100 km. Below Tahiti, *Niu et al.* [2002] find a transition zone thickness anomaly of about 150 km radius. *Wölbern et al.* [2006] determine a plume radius of about 200 km at the 660 km discontinuity beneath Hawaii with a core zone of about 120 km radius. *Montelli et al.* [2004] determine plume radii in the lower mantle in the range 100–

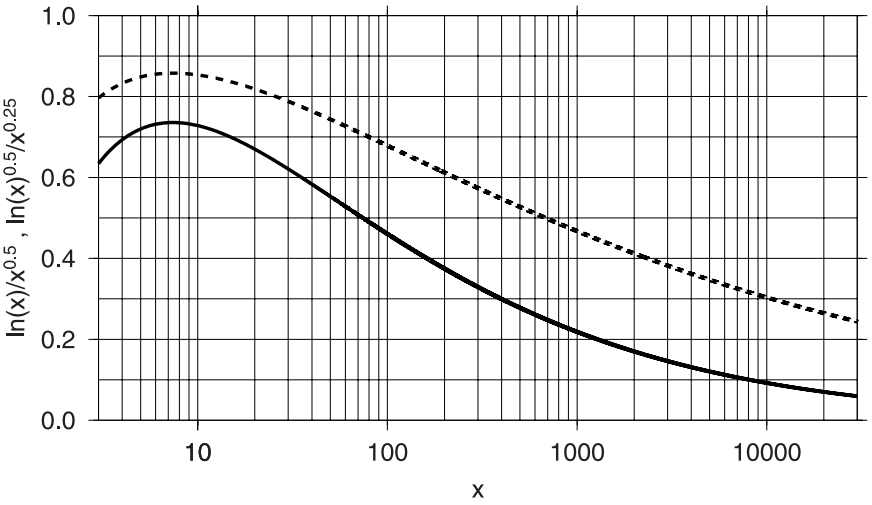

Figure 1. Functions $\ln x/\sqrt{x}$ (solid line) and $\sqrt{\ln x/\sqrt{x}}$ (dashed line), indicating the expected dependence of plume buoyant rising speed and conduit radius on viscosity ratio η_{out}/η_{in}, respectively.

400 km from their tomography model, whereas computations of *Goes et al.* [2004] give plume radii of 150–300 km in the lower mantle. *Constable and Heinson* [2004] find that explaining magnetotelluric seafloor data around Hawaii requires a plume, and its radius appears to be less than 100 km above 150 km depth.

[19] The simplest estimate for plume conduit radius r_c can be made from Poiseuille's formula for flow in a pipe

$$r_c = \left(\frac{8B\eta_{in}}{\pi\Delta\rho dp/dz}\right)^{\frac{1}{4}}. \quad (5)$$

$\Delta\rho$ is the density difference between plume centerline and outside the plume. B is the anomalous mass flux (integral over flow speed times density difference). dp/dz is the pressure gradient available to drive flow through the conduit. It may differ from the hydrostatic value $\Delta\rho\cdot\gamma$. However, this estimate may not be appropriate for determining buoyant rising speed, since the plume conduit is also surrounded by a thermal halo, with a radius larger than the viscous flow radius [*Olson et al.*, 1993]. From *Schubert et al.* [2001], equation (11.9.16) an approximate halo radius of

$$r_c = \left[\frac{1}{\sqrt{2}\Delta\rho\gamma}\cdot\ln\left(\frac{\eta_{out}}{\eta_{in}}\right)\cdot\sqrt{\frac{\eta_{in}}{\eta_{out}}}\cdot\left(\frac{8B\eta_{out}\gamma}{\pi}\right)^{1/2}\right]^{1/2} \quad (6)$$

can be inferred. We assume that heat flux in the plume does not change with depth, therefore

$$B(z) = B_0\cdot\alpha(z)/\alpha(150\text{ km}) \quad (7)$$

with B_0 inferred from observations (section 2.5).

2.4. Rising Speed of Plume Conduit Through Ambient Mantle

[20] Rising speed can be cast in the form of a modified Stokes formula

$$u_b = \frac{k_c\Delta\rho\gamma r_c^2}{\eta_{out}} \quad (8)$$

where k_c is a numerical constant. k_c is larger than the respective value for a fluid sphere because of the interaction of conduit elements. *Richards and Griffiths* [1988] determined $k_c = 0.54$ for a plume that is compositionally different from the surrounding mantle. Inserting equation (6) into (8) gives

$$u_b = \frac{k_c}{\sqrt{2}}\cdot\ln\left(\frac{\eta_{out}}{\eta_{in}}\right)\cdot\sqrt{\frac{\eta_{in}}{\eta_{out}}}\cdot\left(\frac{8Bg}{\pi\eta_{out}}\right)^{1/2} \quad (9)$$

r_c and u_b are approximately independent of η_{in}, when $\ln(\eta_{out}/\eta_{in})/\sqrt{\eta_{out}/\eta_{in}}$ is approximately constant. Figure 1 shows that the function $\ln x/\sqrt{x}$ differs on average less than 10% from the value 0.64 between $x = 3$ and $x = 56$, the range spanned by the experiments of *Kerr and Mériaux* [2004]. Their results are approximately in accord with equation (9) with $k_c/\sqrt{2} \approx 0.54$ ($k_c \approx 0.76$), and hence indicate that thermal plume conduit

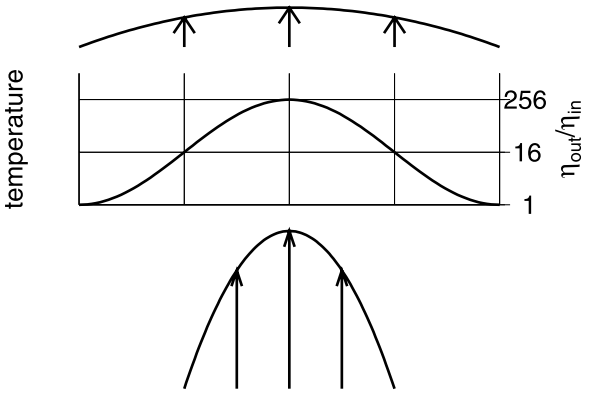

Figure 2. Sketch illustrating why flow restricted to the narrow central part of a plume conduit is effective only if centerline viscosity is substantially reduced. (top) "Wide" Poiseuille flow profile. (middle) Approximate temperature profile across plume. (bottom) "Narrow" Poiseuille flow profile. The narrow and wide profiles correspond to the same flux.

rising speed is almost independent of the viscosity ratio.

[21] This appears surprising at first, since one would expect that a plume with lower centerline viscosity is narrower, hence rises more slowly. However, a qualitative consideration shows that only a substantially lower centerline viscosity will have a noticeable effect on plume thickness. For example, if the flow occurs in a center part with half the total plume radius, on the basis of the Poiseuille formula, an effective viscosity of less than about $(1/2)^4 = 1/16$ of the viscosity of the surrounding material would be required such that flow through the center part becomes more effective than flow through the entire plume (Figure 2). If the temperature anomaly at half the plume radius is half the anomaly at the centerline, and an exponential dependence of viscosity on the temperature anomaly is assumed, the centerline viscosity needs to be reduced by about a factor $(1/16)^2 = 1/256$ relative to the viscosity of the surrounding material such that flow through the narrow central part of the conduit becomes more effective. While the exact number depends on the distribution of temperature in the plume, this qualitative consideration explains the experimental results, but it also suggests that, for viscosity ratios larger than those considered by *Kerr and Mériaux* [2004] (about 56), plumes might still be narrower and buoyant rising speed lower than in the isoviscous case. Figure 1 also shows that for viscosity ratios larger than about 256 buoyant plume rising speeds should be substantially reduced, by a factor 2 or more compared to the value for small viscosity ratios.

[22] Proximity to boundaries will increase viscous drag and hence slow down conduit rising. This effect can be more appropriately considered through a numerical computation of buoyant rising speed as a function of depth, instead of using equation (8).

2.5. Locations, Ages, and Buoyancy Fluxes of Plumes

[23] Both seismic tomography [*Montelli et al.*, 2004] and other arguments [*Courtillot et al.*, 2003] have been used to discern plumes of likely deep mantle origin.

[24] For many plumes, the present location can be presumed to be beneath the end of the respective seamount chain and/or where current or recent volcanism appears to be most active: Easter Island, Kilauea (for Hawaii), Vatnajökull (for Iceland), Marion Island, Piton de la Fournaise (for Reunion), Vailulu'u undersea volcano [*Hart et al.*, 2000] (for Samoa), Mehetia (for Tahiti). For Iceland, this approximate plume location is also supported by crustal thickness [e.g., *Allen et al.*, 2002] and seismic tomography [e.g., *Hung et al.*, 2004]. For Tristan, recent volcanism is documented for both Tristan da Cunha and Gough Island. For New England, Louisville and St. Helena hot spots no recent volcanism is documented, and the location can be inferred from geometry and ages of related seamount chains. For Louisville, a location further south than inferred from the seamount chain is suggested by the hot-spotting technique [*Wessel and Kroenke*, 1997]. The current location of the Kerguelen hot spot is rather uncertain. A location beneath the northwestern Kerguelen plateau had been previously invoked to explain the geometry of the Ninetyeast ridge assuming hot spot fixity. However, there is little observational support for such a present-day hot spot location. On the basis of seamount locations and age data, *Weis et al.* [2002] propose an age-progressive hot spot track between Kerguelen and Heard Island and suggest that the Kerguelen mantle plume may be currently located beneath Heard Island, which features present-day volcanic activity and is located about 1000 km southeast of Kerguelen Island.

[25] The ages of Kerguelen, Louisville, Marion, Reunion and Tristan hot spots can be inferred from radiometrically determined ages of Rajmahal Traps [*Coffin et al.*, 2002], Ontong Java Plateau [*Fitton et al.*, 2004, and references therein], Karoo flood

basalts [*Duncan et al.*, 1997], Deccan traps [*Hofmann et al.*, 2000] and Etendeka Basalts [*Renne et al.*, 1996] which have been associated with the respective plumehead. For Louisville, a younger age is also possible since its association with the Ontong Java Plateau is questionable [*Ingle and Coffin*, 2004; *Korenaga*, 2005b]. For Easter and Hawaii, tracks end at a subduction zone and ages are hence unknown. The Iceland plume is linked to the north Atlantic flood basalt province, but the arrival of the plumehead beneath Greenland may predate it. No flood basalts have been associated with the New England, Samoa and St. Helena hot spots. Ages can be estimated on the basis of radiometric dating [*Gilbert and Foland*, 1986; *Hart et al.*, 2004; *O'Connor and le Roex*, 1992] and the length of the volcanic chains.

[26] *Ribe and Christensen* [1999] point out that previous work [*Davies*, 1988; *Sleep*, 1990] overestimates buoyancy flux of plumes beneath fast-moving plates primarily because the previous estimates were based on the assumption that plume material moves downstream at the same speed as the plate. They determined 2200 kg/s $< B_0 <$ 3500 kg/s for Hawaii, a factor 2 to 3 lower than previous estimates. In analogy, the assumed mass flux of other hot spots beneath fast-moving plates in the Pacific hemisphere (Easter, Louisville, Samoa, Tahiti) should also be lower than previously estimated. Previous flux estimates for hot spots beneath slow-moving plates [*Davies*, 1988; *Sleep*, 1990; *Schilling*, 1991] should be less biased. Plume buoyancy flux estimates in the Pacific hemisphere were previously on average much larger than in the African hemisphere, and this asymmetry is compensated by reducing buoyancy fluxes in the Pacific hemisphere.

2.6. Observations, Experiments, and Numerical Models Regarding Motion of Hot Spots and Shape of Plume Conduits

[27] Numerous observations to which modeling results can be compared to have been compiled in previous work [e.g., *Steinberger*, 2000]. In recent years, new observations have become available to which both the predicted hot spot motion and the predicted plume conduit shapes can be compared to. New age dates [e.g., *Tarduno et al.*, 2003; *Koppers et al.*, 2004] and paleolatitudes [e.g., *Tarduno et al.*, 2003; *Antretter et al.*, 2002] along hot spot tracks can give information on hot spot motion. The predicted shape of plume conduits can be compared to seismic velocity anomalies and transition zone thickness anomalies [e.g., *Montelli et al.*, 2004; *Shen et al.*, 2002; *Hung et al.*, 2004; *Niu et al.*, 2002; *Li et al.*, 2000; *Wölbern et al.*, 2006].

[28] A plume source at the top of a low-viscosity D″ layer may either move with the horizontal flow component at that depth (as assumed in most of our previous work), or be fixed. The latter might be the more appropriate assumption if the plumes rise from the top of a chemically distinct layer at the base of the mantle [*Jellinek and Manga*, 2002; *Davaille et al.*, 2002]. Such a layer would be piled up below upwellings in the overlying mantle, and restoring forces along the tilted interface could substantially reduce horizontal flow speeds compared to the case of a mantle without chemical layering. The convection calculations of *McNamara and Zhong* [2004], though, do not show a large difference between hot spot motion in cases with and without chemical layering. They found that in all cases plume velocities are significantly smaller than typical convective velocities. The slow hot spot motions computed in these convection calculations may be partly due to plumes preferentially being located at stagnant points between downwellings [*Zhong et al.*, 2000]. In our computations, we match present-day observed hot spot locations, which are often not near flow stagnation points.

3. Overview of Numerical Model

[29] We compute the motion of a plume conduit in mantle flow, assuming the velocity of each conduit element is the vector sum of ambient large-scale mantle flow and vertical buoyant rising velocity.

[30] Computation of large-scale mantle flow uses the model smean by *Becker and Boschi* [2002] for relative s-wavespeed anomalies $\delta v_s/v_s$. These are converted to relative density anomalies ($\delta\rho/\rho$). The conversion factor ("Model 2" of *Steinberger and Calderwood* [2006], Figure 3), is depth-dependent but remains close to 0.25 throughout most of the mantle, similar to *Karato* [1993]. Depth profiles for density $\rho(z)$ and gravity $\gamma(z)$ are determined from PREM [*Dziewonski and Anderson*, 1981]. The two ambient mantle radial viscosity profiles $\eta_{\text{out}}(z)$ used are also adopted from *Steinberger and Calderwood* [2006] and shown in Figure 3. Our reference case uses profile 1.

[31] Other details of the computation are the same as given by *Steinberger et al.* [2004], unless specifically noted, the main difference to previous work being the computation of buoyant rising

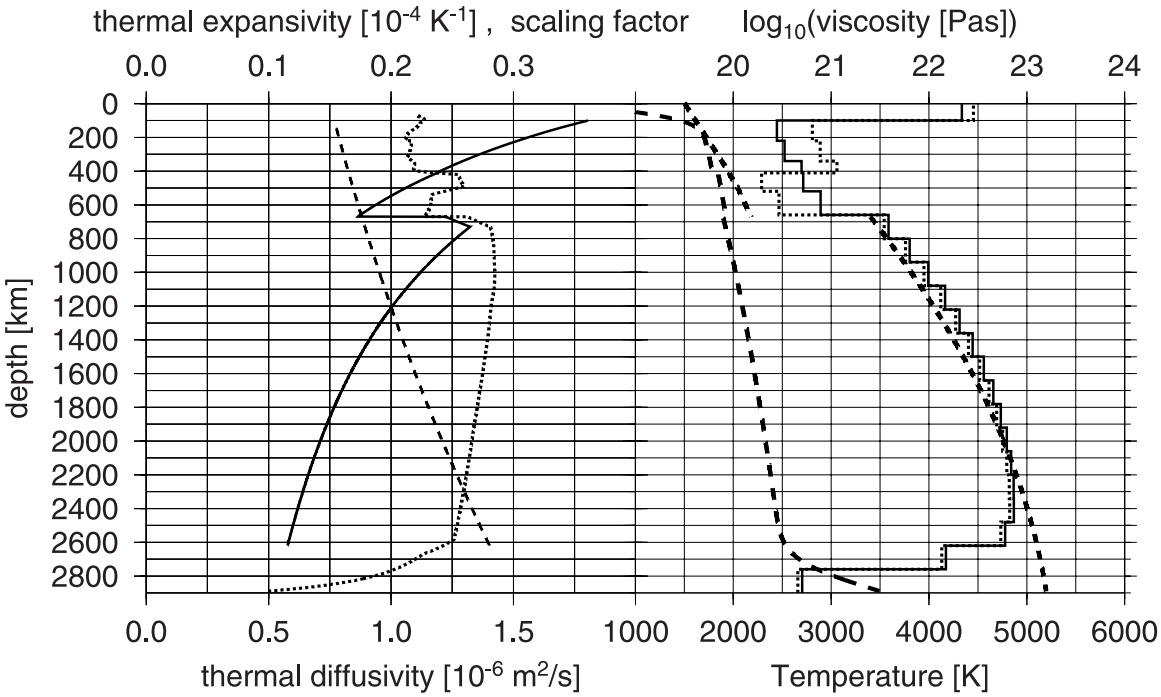

Figure 3. Input profiles used. (left) Thermal expansivity (top scale, solid line), conversion factor from density to seismic velocity anomalies (top scale, dotted line) and thermal diffusivity (bottom scale, dashed line). (right) Ambient mantle viscosity profiles 1 and 2 (top scale, solid line and dotted line), radial temperature profile in ambient mantle $\overline{T}$ (bottom scale, long-dashed line) and profile of $H/(12nR)$ (bottom scale, short-dashed line) with $n = 3.5$ in the upper mantle and $n = 1$ in the lower mantle, where it is identical to the melting temperature profile.

speed. We assume the base of the conduit is at depth 2620 km (top of a low-viscosity layer at the base of the mantle) and either moves with the horizontal flow component at that depth, or is fixed there.

[32] Hot spots modeled are listed in Table 1. The list is based on work discussed in section 2.5 and previous work [*Steinberger*, 2000; *Steinberger et al.*, 2004] and is meant to represent hot spots that (1) have likely deep origin and (2) have been modeled in previous work.

Table 1. Hot Spot Names, Locations, Ages, and Anomalous Mass Fluxes B_0 Used[a]

Name	Longitude	Latitude	Age, Ma	B_0, 10^3 kg/s
Easter	−109.3°	−27.1°	60–100	1
Hawaii	−155.3°	19.4°	120	3
Iceland	−17°	64.4°	60–100	1
Kerguelen	69°	−49°	118	1
	67°	−47°		
	71.2°	−51°		
(Heard)	73.5°	−53.1°		
Louisville	−138.1°	−50.9°	121	1
	−141.2°	−53.5°	(90)	
Marion	37.8°	−46.9°	182	1
New England	−32°	28°	124	1
Reunion	55.7°	−21.2°	65	1
Samoa	−169.1°	−14.2°	40	1
St. Helena	−10°	−17°	100	1
Tahiti	−148.1°	−17.9°	5–20	2
Tristan	−11.3°	−38.7°	132	1

[a] Lines 5–7 are alternative locations for the Kerguelen hot spot. Line 9 gives alternative location and age for Louisville.

[33] Buoyant rising velocity is computed in the four steps (1) temperature anomaly, (2) viscosity, (3) radius, and (4) rising speed of the plume. Whereas we had given a more general background on these in the previous section we explain here specifically our computation.

[34] 1. Temperature anomaly $\Delta T_0(z)$ is computed on the basis of Figure 4 of *Albers and Christensen* [1996]. Temperature anomaly at the base of the plume is 500 K (reference case) or 750 K. We use $C_p = 1250\,\mathrm{J\,kg^{-1}K^{-1}}$ and $\kappa = 0.75 \cdot 10^{-6}\,\mathrm{m^2/s} \cdot 2^{z/z_m}$, whereby z_m is the depth of the mantle such that κ increases by a factor two through the mantle (Figure 3). $\alpha(z)$ is adopted from *Steinberger and Calderwood* [2006] and also shown in Figure 3.

[35] 2. Viscosity ratio η_{in}/η_{out} is computed with equation (4). T_0 is adopted from *Steinberger and Calderwood* [2006] and shown in Figure 3. In the upper mantle, we use $r = 1/3.5$ corresponding to constant strain rate and $n = 3.5$ (dislocation creep) and activation enthalpy $H(z)$ from *Calderwood*

[1999] (Figure 3). In the lower mantle, we use $n = r = 1$, equation (3), $g = 12$ and a melting temperature profile based on experimental results (Figure 3).

[36] 3. Conduit radius $r_c(z)$ is computed with equations (6) and (7). $\Delta\rho(z)$ is computed from $\Delta T_0(z)$ and $\alpha(z)$ profiles and the PREM density profile. Values for B_0 are listed in Table 1.

[37] 4. Conduit rising speed is computed in three steps:

[38] Step a: A synthetic density field representing a tilted plume is computed on the basis of $\Delta\rho(z)$ and $r_c(z)$.

[39] Step b: The flow field for a tilted plume conduit is computed with the same method as large-scale mantle flow [*Hager and O'Connell*, 1979, 1981].

[40] Step c: The maximum upward velocity at each depth level is determined, and used as buoyant plume conduit rising speed. If η_{in} is substantially lower than η_{out} we expect flow through the conduit and hence maximum upward velocity to be faster than buoyant rising speed. However, the *Hager and O'Connell* [1981] method used does not consider lateral viscosity variations; computed upward velocity at each depth level occurs approximately at the center of the temperature anomaly (plume conduit), the computed velocity vector at this location is approximately vertically upward, and in time-dependent calculations the temperature anomaly approximately rises with that speed. Hence computed maximum upward velocity is an appropriate measure of buoyant rising speed. For comparison, buoyant rising speed is also computed with equation (9).

[41] For step a, we consider for the temperature structure in the plume

$$\Delta T = \Delta T_0 \cdot \exp\left[-(x/r_c)^2\right] \tag{10}$$

or

$$\Delta T = \Delta T_0 \cdot \left[1 - (x/r_c)^2\right] \text{ for } x < r_c \text{ and } \Delta T = 0 \text{ for } x > r_c \tag{11}$$

[*Schubert et al.*, 2001, equation (11.9.7)], or the arithmetic mean of the two cases (reference case). x is the distance from the plume center axis, and plume tilts are 0°, 30°, 45° (reference case) and 60° with the vertical. The integral of the temperature anomaly over the plume should approximately determine buoyant rising speed, according to equation (8). This integral is $\Delta T_0 r_c^2 \pi$ with equation (10) and $\Delta T_0 r_c^2 \pi/2$ with equation (11).

[42] For step b, we use a viscosity structure that is the same as for computing large-scale flow, except that viscosity below the lithosphere is reduced by a factor 10000, 1000 (reference case), 100 or 10, or not reduced. In order to be able to resolve plume conduits, we expand here density structure and flow up to spherical harmonic degree $l = 255$ (corresponding to a half-wavelength about 80 km near the Earth surface) and use a fixed upper boundary. In contrast, large-scale mantle flow related to density anomalies derived from seismic tomography is only expanded to $l = 31$. For $l \leq 48$ a free surface at the core-mantle boundary (CMB) at depth 2900 km is used as lower boundary condition. However, for $l > 48$ a fixed surface at depth $(2900 \cdot 48/l)$ km is used instead; higher harmonics at larger depth are not considered. This modification of boundary condition is introduced, because otherwise the computed flow field diverges rather than matching the prescribed (zero) surface velocity. It has a rather small effect on our results, since plumes in the lower mantle are presumably rather thick and expansion up to degree 48 is adequate there. Also, results do not much depend on whether a free or fixed lower surface is assumed. Comparison of results obtained for different expansion (l = 255, 127, 63) suggests that expansion to even higher l will change results only insignificantly.

4. Results

4.1. Resulting Plume Temperature, Density, Seismic Velocity, and Viscosity Anomaly and Radius

[43] The left panel of Figure 4 shows the centerline temperature anomaly versus depth for plumes with three different values of sublithospheric anomalous mass flux and two different basal temperature anomalies. With decreasing depth, the plume cools relative to the ambient mantle even in the adiabatic limit for a very large buoyancy flux: In this case, 500 K starting temperature anomaly reduces to ≈325 K at 200 km depth. Reduction of temperature anomaly beyond that is due to diffusive cooling.

[44] For computation of buoyant rising speed, we convert temperature anomaly to density anomaly (Figure 4, right panel). For the most part, it is

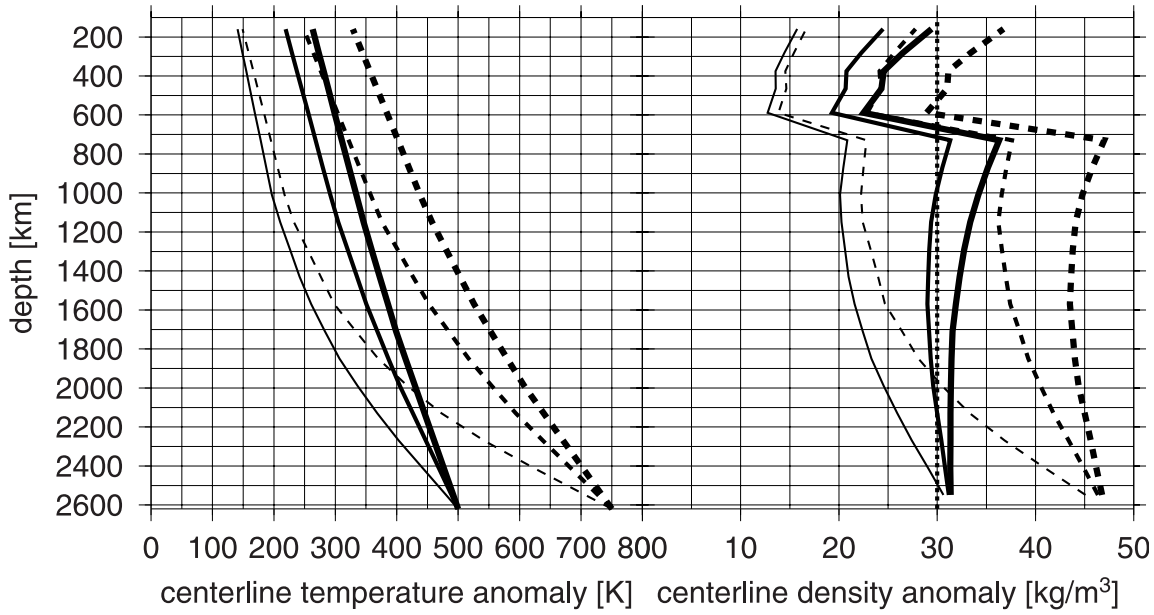

Figure 4. (left) Radial profiles of plume centerline temperature anomalies computed following *Albers and Christensen* [1996] for $B_0 = 10^3$ kg/s (thin lines), $2 \cdot 10^3$ kg/s (medium lines), and $3 \cdot 10^3$ kg/s (thick lines) and 500 K (solid lines) and 750 K (dashed lines) basal temperature anomaly. (right) Centerline density anomaly inferred from temperature anomaly; dotted line at 30 kg/m^3.

similar to 30 kg/m^3, the constant value used in most previous models of plumes in large-scale mantle flow, particularly if a basal temperature anomaly 500 K is assumed.

[45] In the right panel of Figure 5 the viscosity contrast between the plume centerline and ambient mantle is shown. The contrast between plume and surrounding mantle is much higher in the lower mantle than in the upper mantle. One reason for this is that the plume excess temperature drops from the base to the surface. This happens even in the adiabatic case (i.e., in the limit of a very large

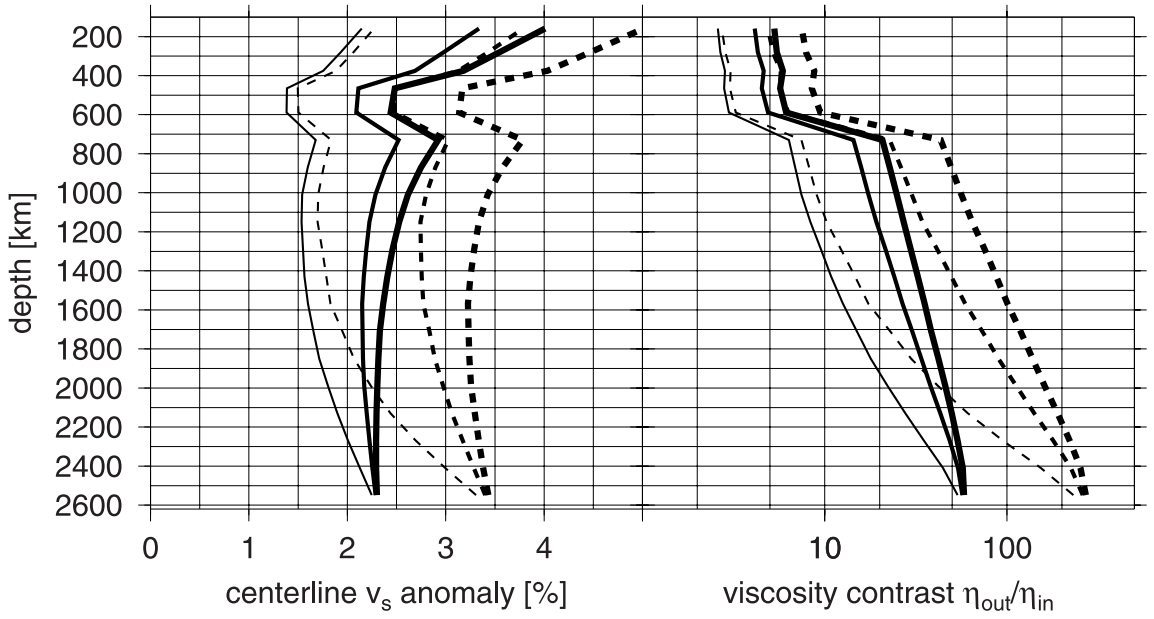

Figure 5. (left) Centerline seismic v_s anomaly inferred from temperature anomaly (Figure 4), using the conversion factors derived by *Steinberger and Calderwood* [2006]. (right) Viscosity contrast η_{out}/η_{in} computed with equation (4), for the same cases as in Figure 4.

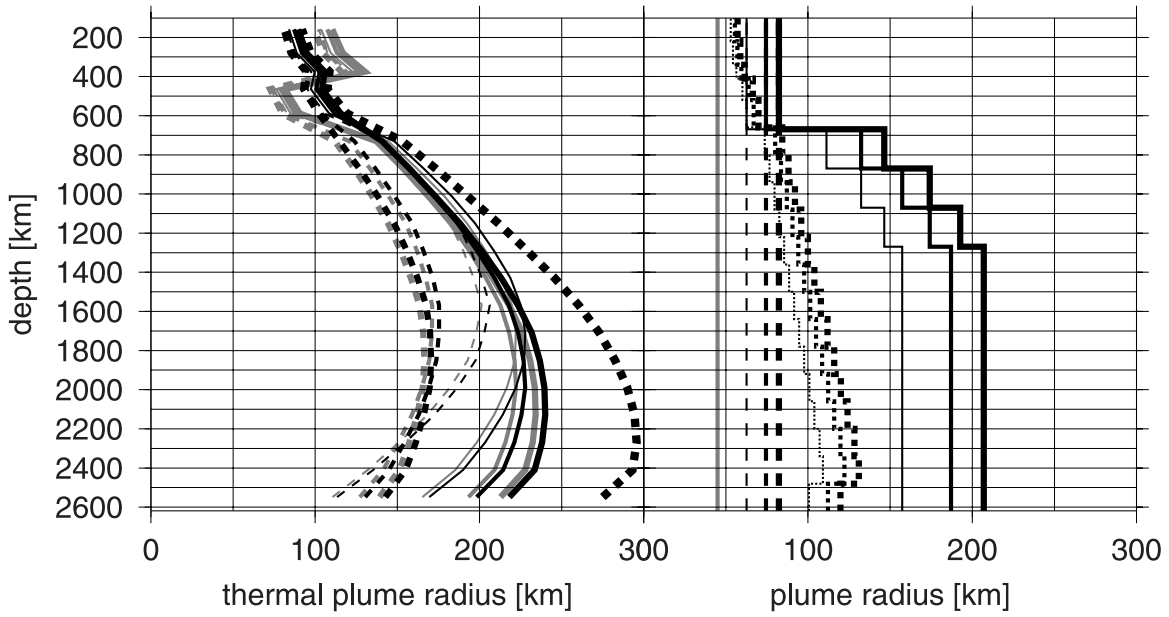

Figure 6. Plume conduit radius as a function of depth. (left) Radii computed with equation (6). Dashed lines are for basal temperature anomaly 750 K; solid lines are for 500 K. Black lines are for ambient mantle viscosity model 1; gray lines are for model 2. Solid and dashed lines are for anomalous mass flux $B_0 = 3 \cdot 10^3$ kg/s (thick lines), $2 \cdot 10^3$ kg/s (medium), and 10^3 kg/s (thin). For the dotted line, $B_0 = 4 \cdot 10^3$ kg/s, and $\ln(\frac{\eta_{out}}{\eta_{in}}) \cdot \sqrt{\frac{\eta_{in}}{\eta_{out}}}$ has been replaced by its maximum value, 0.736. (right) Previous assumptions. Gray line, *Steinberger and O'Connell* [1998]; dashed lines/solid black lines, models 1 and 2 of *Steinberger* [2000]; dotted lines, *Steinberger et al.* [2004]. For the last three cases, anomalous mass fluxes are as in the left panel.

plume), but even more so for smaller plumes. The other reason is that we use different rheological laws in the upper and lower mantle. However, appropriate mantle rheology and hence viscosity contrast η_{in}/η_{out} remain rather uncertain. The effect of multiplying H/nR with a constant amounts to scaling these curves (with logarithmic horizontal scale) in horizontal direction. The effect on conduit rising speed and radius can then be inferred from Figure 1. Because through considering different starting temperature anomalies and mass fluxes we already cover a wide range of viscosity contrasts plume versus surroundings and are able to assess its effect on our results, we will not consider different values for other parameters that enter the computation.

[46] Results for plume conduit radius are shown in Figure 6. For viscosity profile 1, plume conduit radius in the upper mantle is about 100 km and slightly increases with depth, and is rather independent of other model assumptions. For viscosity profile 2, though, predicted conduit radius is smaller in the transition zone (about 70 to 80 km) than in the upper mantle (100–120 km). For a starting temperature anomaly of 500 K we find plume conduit radii in the lower mantle of about 200 km, with the maximum radius occurring in the mid-lower mantle.

[47] We also compute the radius for a large plume with $B_0 = 4 \cdot 10^3$ kg/s and high viscosity, replacing $\sqrt{\ln(\eta_{out}/\eta_{in}) \cdot \sqrt{\eta_{in}/\eta_{out}}}$ in equation (6) by its maximum value 0.8577 (Figure 1). This increases the plume radius in the lower mantle to up to 300 km.

[48] For viscosity profile 1, there is no big difference in plume radius above and below 660 km. This occurs, because in equation (6) the difference due to ambient mantle viscosity η_{out} above and below is approximately compensated by the difference due to viscosity contrast η_{out}/η_{in}, and this is in turn due to the different rheological law assumed. The right panel of Figure 6 shows radii for previous models.

4.2. Resulting Plume Conduit Rising Speed

4.2.1. Calibration With Experimental Results

[49] In order to determine whether equation (10) or (11) is more appropriate for temperature structure in the plume, we first compute buoyant rising

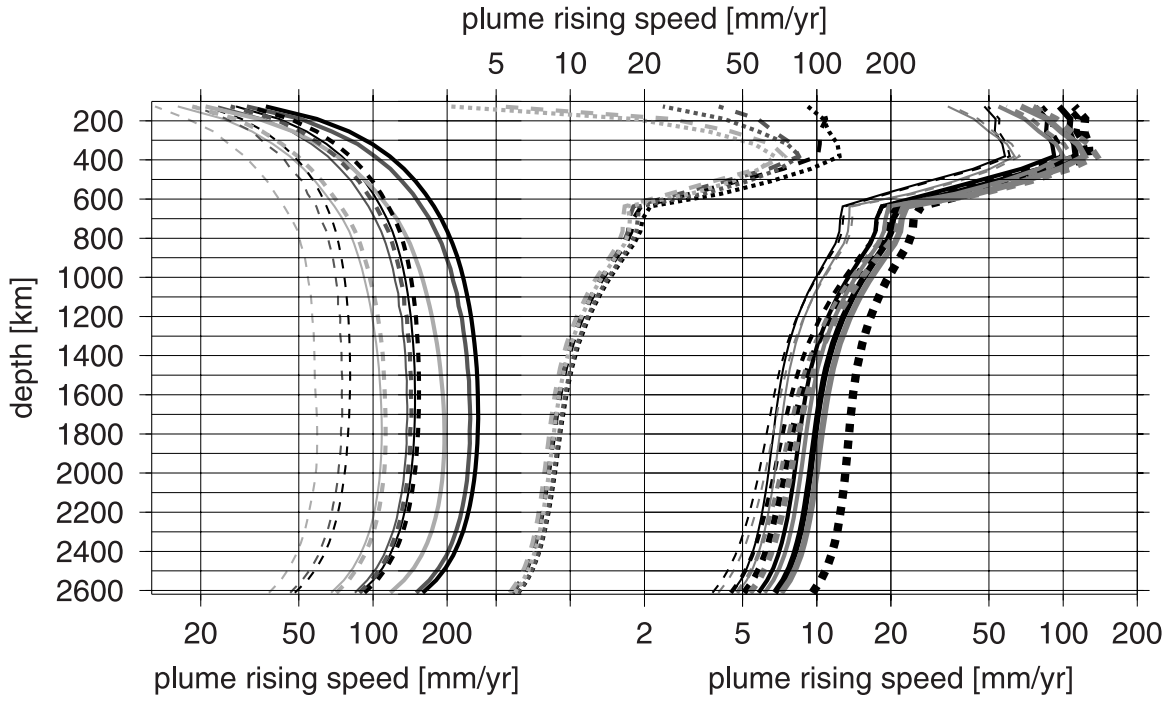

Figure 7. Plume conduit buoyant rising speed computed with *Hager and O'Connell* [1981] method. Left bottom scale: "Calibration" cases with constant ambient mantle viscosity and plume radius; plume temperature structure as in equation (10) for solid lines and equation (11) for dashed lines. Thick lines are for thermal plume radius 137 km; thin lines are for 97 km. Vertical plume for black lines, plume tilted 30° from vertical for dark gray, 60° for light gray lines. Middle top scale: Viscosity reduced between 100 and 127 km depth by factor 10000 (black lines), or 100 (dark gray lines), or not reduced (light gray lines), and mantle viscosity models 1 (dashed lines) and 2 (dotted lines) elsewhere, tilt 45°, basal temperature anomaly 500 K, anomalous mass flux $B_0 = 2 \cdot 10^3$ kg/s. Right bottom scale: Same cases as in the left panel of Figure 6, tilt 45°, viscosity reduced by a factor 1000 between 100 and 127 km depth; arithmetic mean between the two cases on radial plume structure.

speed for a case that can be compared with the experimental results of *Kerr and Mériaux* [2004]: constant ambient viscosity 10^{21} Pas, incompressible mantle with density 4449 kg/m^3, no phase boundaries, constant gravity 10 m/s^2, constant plume density anomaly 1%. We consider cases with plume tilt of 0°, 30° and 60° with the vertical, radial plume structure from equations (10) and (11) and r_c = 97 km and 137 km. Scaled to the depth of the layer, these radii approximately correspond to those in Table 4 of *Kerr and Mériaux* [2004], and equation (8) with k_c = 0.76 yields u_b = 100 mm/yr for r_c = 97 km and 200 mm/yr for 137 km, i.e., these are the values inferred by scaling the experimental results of *Kerr and Mériaux* [2004] to Earth dimensions. Results shown in the left panel of Figure 7 indicate that rising speeds computed with plume temperature structure from equation (10) are (with the exception of the case with tilt 60° and r_c = 137 km) higher in the mid-mantle than the value computed with equation (8) and k_c = 0.76, and those computed with equation (11) are lower. For tilts 0°, 30° (approximately bracketing the tilts in the experiments of *Kerr and Mériaux* [2004]), the arithmetic mean for the two temperature structures is in the mid-mantle quite close to the value computed with equation (8). Therefore, in the following, we shall always use the arithmetic mean of the rising speed computed for the two cases, which is an appropriate choice if the radial plume temperature structure in the Earth mantle is similar to that in the experiments of *Kerr and Mériaux* [2004].

4.2.2. Results With "Earth-Like" Viscosity Structure

[50] In the vicinity of plumes, viscosity beneath the lithosphere is expected to be reduced relative to the underlying mantle because of plume material flowing out of the conduit, and buoyant plume rising speed in the uppermost mantle depends on whether such a low-viscosity channel exists below the lithosphere, and if so, with which viscosity. Figure 7 also shows rising speeds computed with

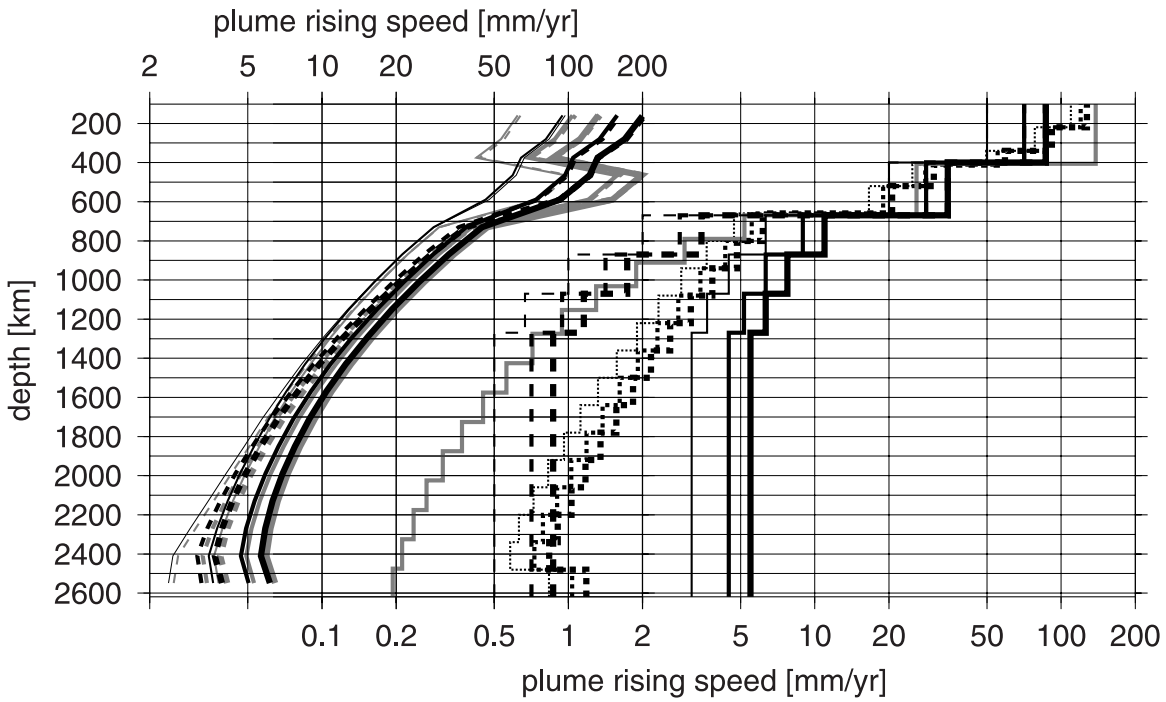

Figure 8. Plume conduit buoyant rising speed computed with equation (8). Left top scale: Same cases as in the left panel of Figure 6, with k_c = 0.76. Right bottom scale: Previous models with k_c = 0.54, as in the right panel of Figure 6.

the *Hager and O'Connell* [1981] method with a 27 km thick layer where viscosity is reduced by a factor 100 or 10000 relative to the mantle beneath, and without such a layer; results for a factor 1000 reduction are shown in the right panel. In this case, we obtain buoyant plume rising speeds of about 5–10 cm/year beneath the lithosphere, i.e., plume rising speed is not substantially reduced due to the proximity of the lithosphere. Without decoupling layer, rising speed substantially slows down close to the lithosphere.

[51] Comparison with the left panel of Figure 8 shows that rising speeds computed with the *Hager and O'Connell* [1981] method are larger than those computed with equation (8) in the lower mantle below about 1600 km and generally smaller above that depth. This occurs because plume buoyant rising velocity is not only determined by the local viscosity, but viscosities in the whole mantle, which tends to smooth out variations in u_b. Comparison of the right panels of Figures 7 and 8 shows that the rising speeds in model 2 of *Steinberger* [2000] are quite similar to those in our reference case in the upper mantle, somewhat less in the lowermost mantle, and up to about a factor 2 less in the mid-mantle. Rising speeds in other previous models, e.g., model 1 of *Steinberger* [2000] tend to be less in the lower mantle. Nevertheless, models 1 and 2 of *Steinberger* [2000] resulted in very similar hot spot motion and plume conduit shape: hot spot motion most frequently tends to be similar to the horizontal flow component at a depth for which the buoyant rise time (Figure 9) is similar to plume age [*Steinberger*, 2000], and this is quite similar (≈600–1000 km) for both models for most times. Figure 9 shows that, for the plume models of this paper, for plumes older than ≈10 Ma, this depth tends to be in the lower mantle, increasing with age, and somewhat deeper than in our previous models. How much modeled hot spot motion differs from our previous work will therefore, among other things, depend on how much the direction of flow in the mid-mantle changes with depth.

4.3. Computed Conduit Shape for Tahiti: Calibration of Asthenosphere Viscosity by Comparison With Observations

[52] We first discuss the effect of plate motions on conduit shape which is particularly important below fast-moving plates, such as the Pacific plate. In Figure 10 we show results for the computed

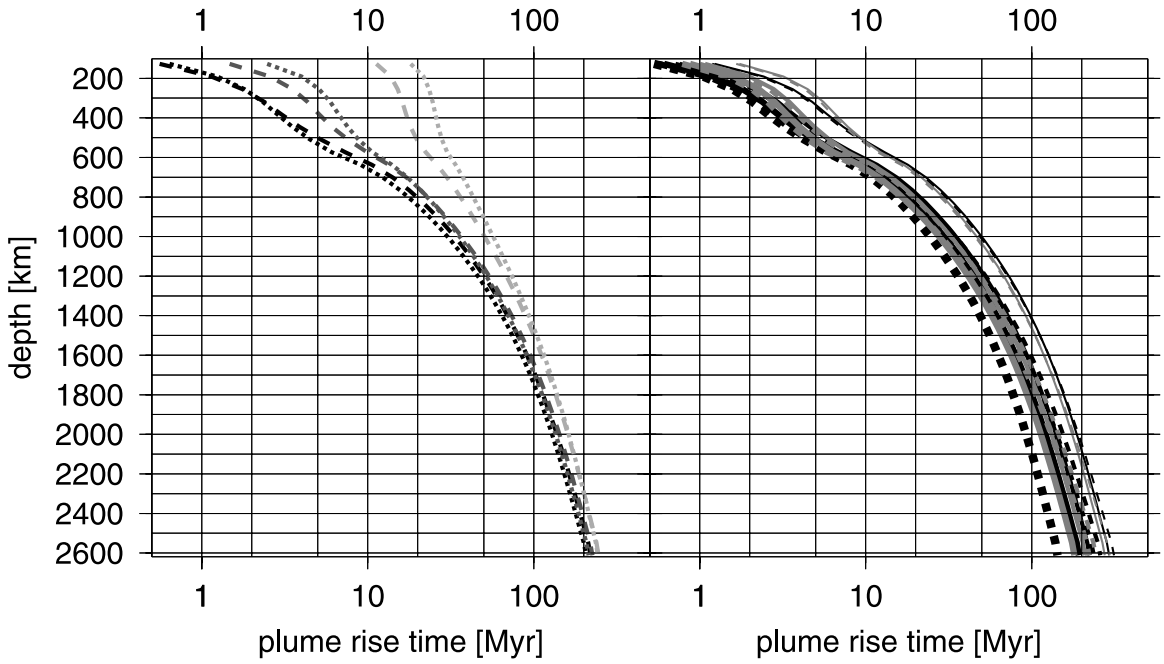

Figure 9. Plume conduit buoyant rise time from a given depth to the surface (i.e., depth integral over $1/u_b$) for cases as in the middle and right panels of Figure 7.

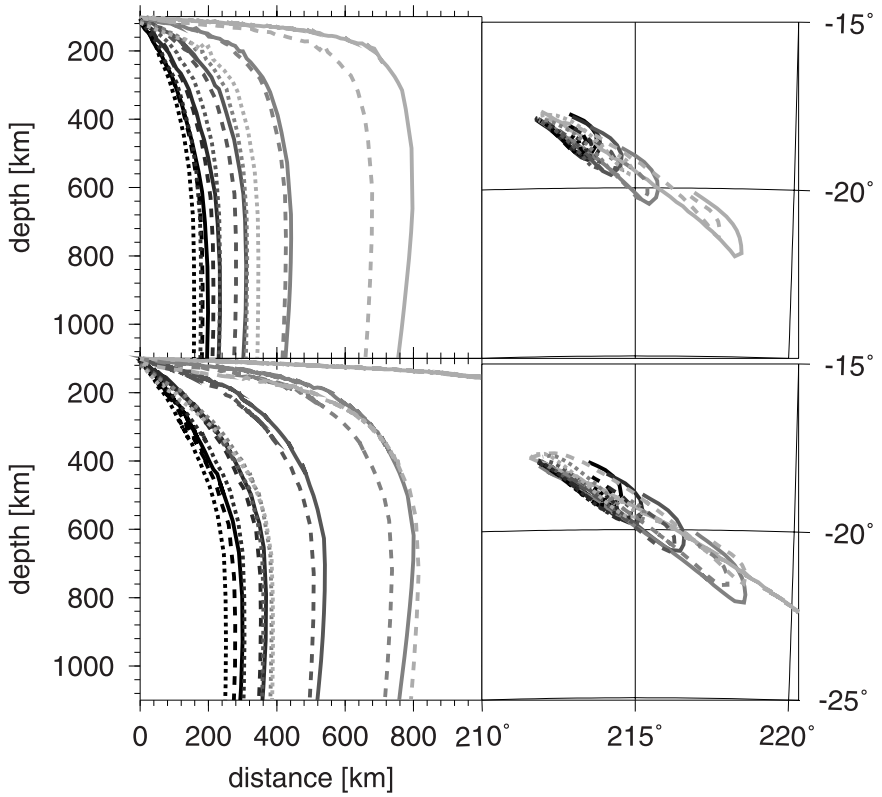

Figure 10. Computed plume conduit shape of the Tahiti hot spot. Top panels are for viscosity profile 1; bottom panels are for profile 2. Left panels show the horizontal distance between plume conduit location at depth and surface hot spot; right panels are map views of the conduit. Dotted, dashed, and solid lines are for plume conduit initiation ages 5, 10, and 20 Ma. Viscosity between depth 100 and 127 km is reduced by factor 10000, 1000, 100, 10, or 1, darker colors corresponding to stronger viscosity reduction. Plume temperature anomaly at base is 500 K.

conduit shape of the Tahiti hot spot, which is a good candidate for deep mantle origin [*Montelli et al.*, 2004]. *Niu et al.* [2002] find a region of transition zone thinning (the likely location of the plume conduit at transition zone depth) centered about 200 km East of Mehetia, the presumed surface location. Figure 10 (top left panel) shows that this is approximately matched by the computed offset in our reference case with a factor 1000 viscosity reduction beneath the lithosphere. If there is less viscosity reduction (lighter colored curves), the computed offset tends to be larger. This is especially so for the older assumed plume initiation ages (dashed and solid lines). Since the computation is started with an initially vertical conduit, the conduit tilt due to plate motion has not yet reached its steady-state value for younger ages and less viscosity reduction. Because of the absence of any indication of a large plumehead, we regard it however as more likely that the conduit already had an approximately steady-state tilt in the uppermost mantle at ≈5 Ma, the time of the oldest volcanics. The absence of a plumehead does not necessarily preclude a deep mantle origin [*Farnetani and Samuel*, 2005], and the computed steady-state shape in the upper mantle is almost independent of the assumed depth of plume origin. Also, the approximately linear age progression [*Duncan and Clague*, 1985] gives no indication of a initial adjustment of conduit shape [*Steinberger*, 2000]. Hence we regard it as more appropriate to use the older plume initiation ages in the computation, as they yield an approximately steady-state tilt of the plume conduit due to plate motions for the times ≈0–5 Ma represented in the hot spot track. A somewhat larger displacement is also computed with viscosity profile 2 (Figure 10, bottom left panel), because in this case the uppermost mantle is more viscous than the transition zone, hence gets more dragged along with the moving plate, and the conduit gets more advected in this layer. The right panels show that the computed surface hot spot position is offset relative to its location in the transition zone toward the west-northwest, in the direction of plate motion, whereas the offset inferred from observations is toward the west.

[53] Similar results were obtained for the Hawaiian hot spot; in our reference model shown in Figure 13 the conduit is in the transition zone about 200 km southeast of the surface hot spot. For less viscosity reduction below the lithosphere, the offset again becomes larger, and more toward the east-southeast, corresponding to the plate motion direction. This increases the discrepancy with the results of *Li et al.* [2000] and *Wölbern et al.* [2006] who infer a location about 200 km toward the southwest. Since the direction of this offset is approximately orthogonal to the plate motion direction, it indicates that the tilt due to plate motion cannot be very large.

[54] Similarly, *Richards and Griffiths* [1988] show that if the bend in the Hawaiian-Emperor chain is due to a change in plate motion, an interpretation that is not universally agreed upon, its sharpness indicates that the plume conduit is tilted over due to plate motion by less than about 200 km, and adjustment of conduit shape to plate motion change took approximately 3 Myr or less. Figure 10 shows that most of the adjustment of the conduit to plate motions occurs between about 100 and 400 km in our model, hence the buoyant risetime from depth 400 km should approximately correspond to the time of conduit shape adjustment to plate motion changes. The right panel of Figure 9 yields a risetime of about 3 Myr for Hawaii, whereas for substantially less viscosity reduction (Figure 9, left panel) adjustment times would be much larger.

[55] We therefore regard results of conduit tilt due to plate motions obtained with a factor 1000 viscosity reduction below the lithosphere as appropriate, whereas a substantially smaller reduction gives conduit tilts and adjustment times too large to be compatible with observations. Corresponding asthenosphere viscosities in the vicinity of plumes are between 10^{17} and 10^{18} Pas, in agreement with other work [*Schubert and Hey*, 1986; *Albers and Christensen*, 2001].

4.4. Computed Motion of Other Hot Spots and Comparison With Previous Results

[56] Figure 11 shows computed hot spot motion for our reference model and a moving plume source. Since conduit rise times from the lowermost mantle (Figure 9) are larger than assumed plume ages, assumptions about motion of the base of the plume influence computed hot spot motion only for sufficiently old hot spots where conduit elements initially at the base of the mantle have risen to the surface aided by upward large-scale flow. In our computations, this occurs only for Hawaii, Iceland (age 100 Ma), Kerguelen, and Marion. For other hot spots, computed hot spot motion is the same for fixed and moving source, for Iceland (100 Ma) it is very similar. For Hawaii, Kerguelen and Marion, computed hot spot motion with a fixed source is very similar to Figure 12.

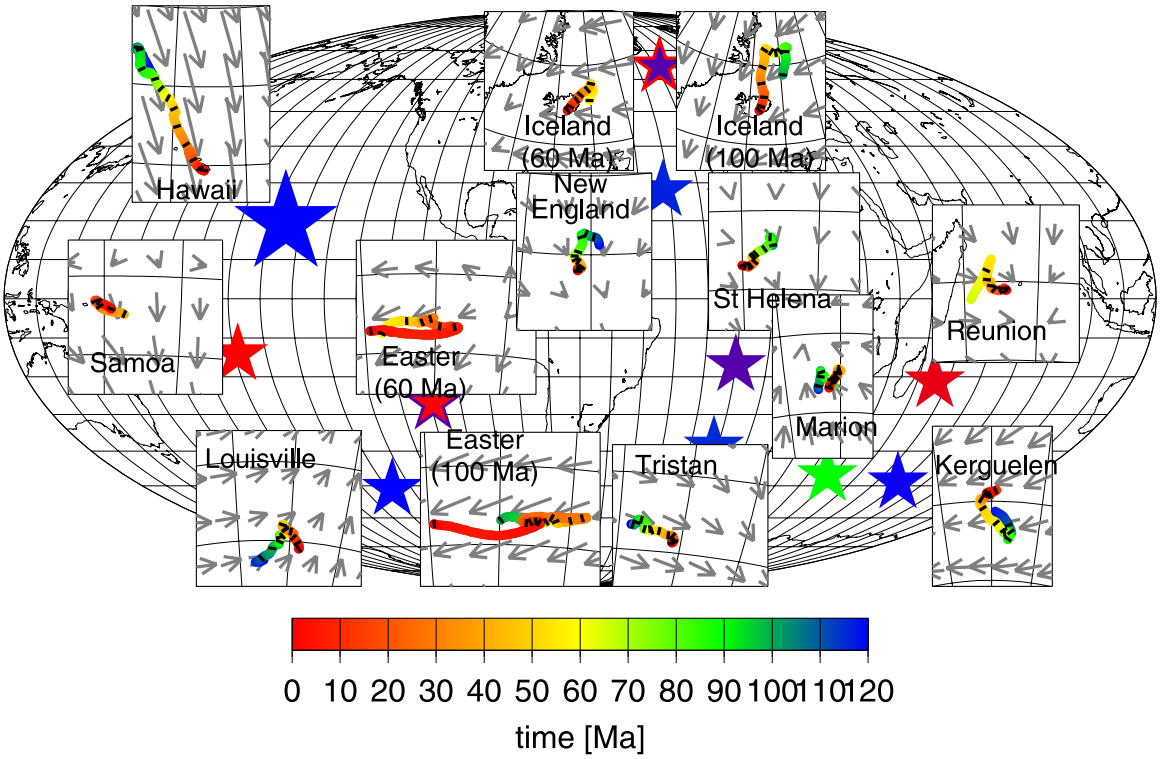

Figure 11. Computed hot spot motions with viscosity model 1 and temperature anomaly 500 K at plume base. Also included is the horizontal flow component at depth 933 km for Samoa, 1077 km for Easter (60 Ma) and Iceland (60 Ma), 1220 km for Reunion, 1507 km for St. Helena, Easter (100 Ma), and Iceland (100 Ma), 1651 km for Louisville, Tristan, New England, and Kerguelen, and 2081 km for Marion and Hawaii. Arrow length scale is 5 degrees of arc per cm/yr; grid spacing is 10 degrees here and in the following figures.

[57] Computed hot spot motions are, in most cases, within the range of, and quite similar to previous results [*Steinberger and O'Connell*, 1998, 2000; *Steinberger*, 2000, 2002; *Antretter et al.*, 2002, 2004; *Tarduno et al.*, 2003; *O'Neill et al.*, 2003, 2005; *Hart et al.*, 2004; *Koppers et al.*, 2004; *Steinberger et al.*, 2004], and most previous comparisons with observations remain valid. In general, because buoyant plume rising speed is somewhat faster than in previous models, computed hot spot motion tends to represent flow at somewhat larger depth, somewhat more toward (or less away from) the large-scale upwellings beneath the Pacific and Africa. For comparison, Figure 11 shows for each plume the horizontal flow component at a depth for which plume conduit buoyant rise time (Figure 9) is approximately equal to the age of the plume (Table 1).

[58] Apart from the results shown, computations for all hot spots were performed with anomalous mass flux 1000 kg/s, 2000 kg/s and 3000 kg/s, basal temperature anomaly 500 K and 750 K, viscosity models 1 and 2, and two methods of computing buoyant plume rising speed, and results remain similar in most cases.

[59] Furthermore, we also computed results corresponding to the thick dotted lines in Figures 6, 7, and 9. They represent plumes with viscosity similar to the surrounding mantle, and a high anomalous mass flux consistent with dynamic thermal plume models, on the upper end of observation-based estimates. Results are shown in Figure 12 for the six plumes with assumed age of more than 100 Ma. For these "old" plumes, whether their source is fixed or moves starts to influence surface hot spot motion at some time before the present: For moving plume sources, computed hot spot motion over the past few tens of Myr tends to represent flow in the lowermost mantle, generally toward the large-scale upwellings beneath Pacific and Africa, but for fixed sources it tends to be in a different direction, and total predicted hot spot motion tends to be less than for a moving source. For younger plumes, computed hot spot motions are identical for both cases and mostly similar to those shown in Figure 11.

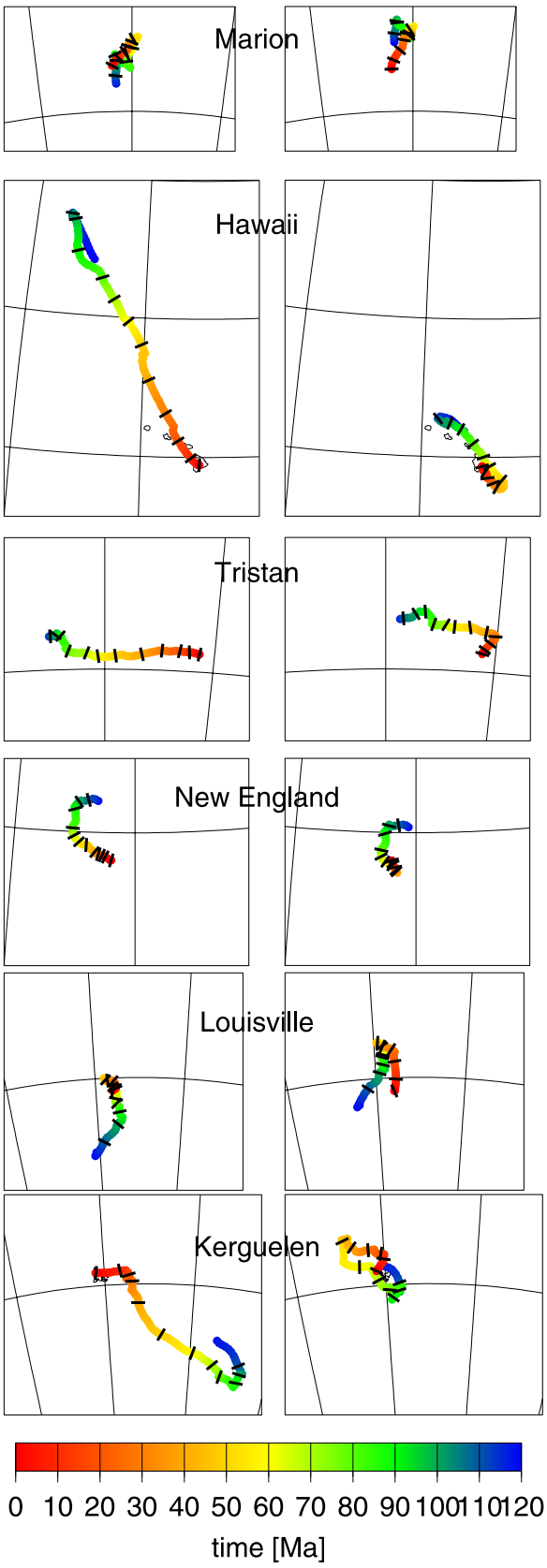

Differences to results shown in Figure 11 tend to be larger for older plumes. This is expected from Figure 9, because differences between the thick dotted line and other lines become larger for larger times and depths.

4.5. Computed Conduit Shape for Moving and Fixed Plume Sources

[60] Computed plume shape is quite different for moving and fixed sources: Conduit shapes with a moving plume source are shown in Figure 13, with a fixed plume source in Figure 14. Moving plume sources tend to be displaced relative to the hot spot surface locations toward the center of the two large-scale upwellings under the Pacific and Africa, due to inward flow toward these upwellings at the base of the mantle (shown at depth 2512 km in Figure 13). In most previous work, a moving source was assumed, and results obtained here are very similar to those previous results. If plume sources are fixed, the conduit leaving the fixed source tends to get advected with the lower-mantle flow (shown at depth 1938 km in Figure 14) toward the large-scale upwelling, and the predicted direction of plume tilt in the lowermost mantle tends to be reversed relative to the case of a moving source, and relative to the predicted tilt in the upper part of the mantle. Conduit shapes were computed for the same cases as hot spot motion, and results are again very similar regardless of assumed anomalous mass flux, basal temperature anomaly, viscosity model, and method of computing buoyant plume rising speed. Even for the case shown in Figure 12, computed conduit shapes remain rather similar and are therefore not shown.

4.6. Results for Individual Hot Spots

[61] In the following we point out a few noteworthy features of our new results, and differences to previous results, for individual hot spots:

[62] Hawaii: Computed motion remains in south-southeasterly direction. Since we find that the computed southward motion during the last 80 Myr gets larger for an older assumed age, if a moving source is assumed, we choose an age such that in this case we approximately match the amount of southward motion inferred from paleo-

Figure 12. Computed hot spot motions with viscosity model 1 and conduit rise speed as thick dotted line in Figure 7, with moving (left panels) and fixed (right panels) plume source.

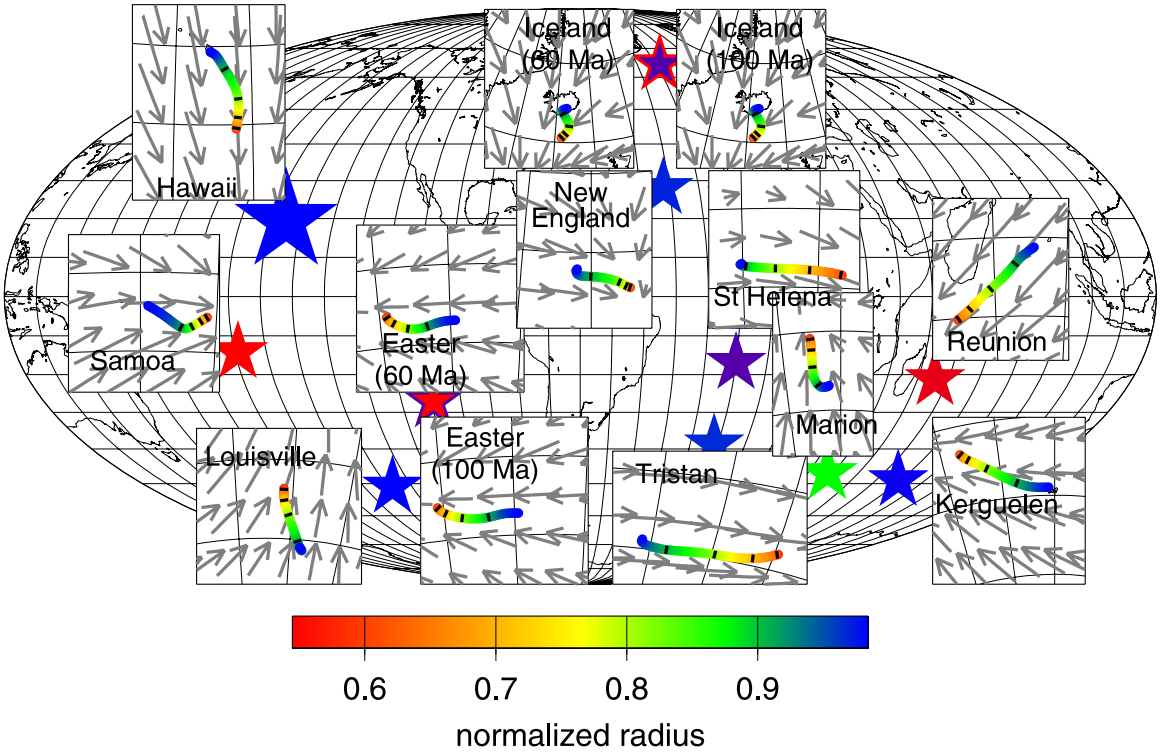

Figure 13. Plume conduit shapes computed for the same case as in Figure 11. Also shown is the horizontal flow component at depth 2512 km, close to the base of the plume. Arrow length scale is 5 degrees of arc per cm/yr.

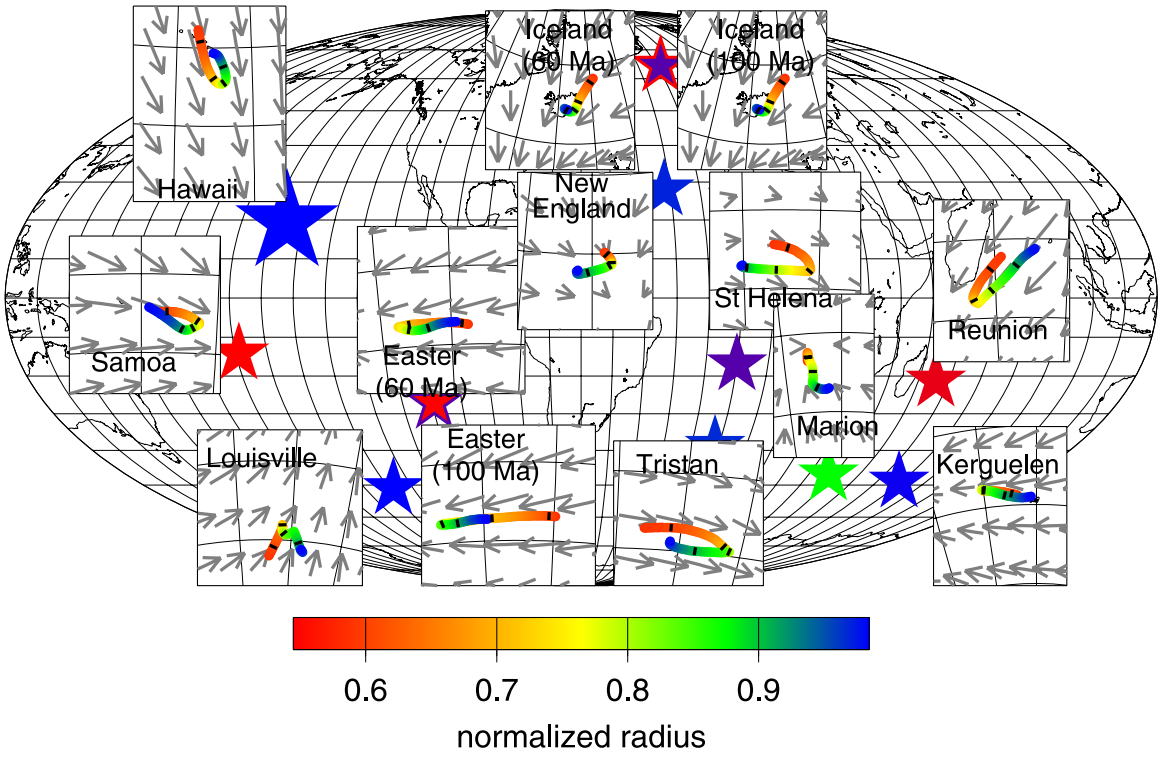

Figure 14. Plume conduit shapes computed with a fixed plume source. Also shown is the horizontal flow component at depth 1938 km. Other modeling assumptions and arrow length scale are the same as in Figure 13.

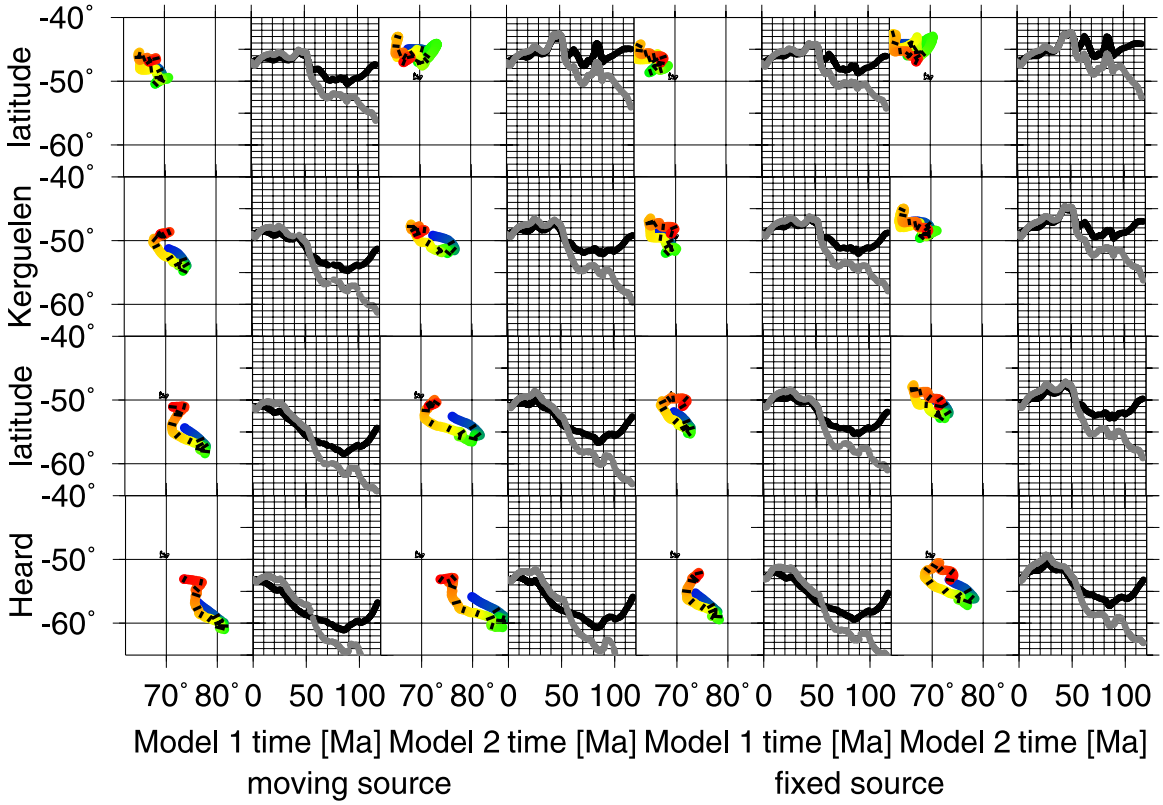

Figure 15. Computed motion and paleolatitudes of the Kerguelen hot spot. Assumed present location beneath the northwestern Kerguelen plateau (67°E, 47°S) in top row, Kerguelen Island (69°E, 49°S) in second row, half-way between Kerguelen and Heard Island (71.2°E, 51°S) in third row, and Heard Island (73.5°E, 53.1°S) in bottom row. Ambient mantle viscosity model 1 (columns 1, 2, 5, 6) or 2 (columns 3, 4, 7, 8); plume source moving (columns 1–4) or fixed (columns 5–8). Paleolatitudes are either computed solely from hot spot motion (black curves) or a combination of true polar wander [*Besse and Courtillot*, 2002] and hot spot motion. Color scale is the same as in Figure 11.

magnetism [*Tarduno et al.*, 2003]. Computed motion is smaller for a fixed source.

[63] Iceland: We had previously assumed a plume initiation age 60 Ma. This yielded an overall slow hot spot motion approximately westward. A similar result is obtained here. However, the Iceland plume may predate opening of the North Atlantic, and hence we include here also a result for age 100 Ma. In this case, predicted hot spot motion is more toward the south, reflecting the flow direction at larger depth. Predicted conduit shape is very similar to previous results in both cases.

[64] Kerguelen: Results for a number of cases are shown in Figure 15. Whereas most previous models tended to predict Kerguelen hot spot motion in southeasterly direction, this is not a general feature of our new results: Assuming a moving hot spot source, overall hot spot motion, especially during the last 100 Myr, tends to be rather toward the northwest, opposite to previous results. This motion represents flow in the lower part of the mantle, and the higher buoyant rising speed is assumed, the larger computed motion gets (compare Figure 12 and Figure 11). During the past few tens of Myr motion of the source in a west-northwest direction also contributes to hot spot motion. Hence computed hot spot motion is smaller, if a fixed source is assumed. Also, the further northwest the hot spot location is assumed, the smaller this northwestward motion becomes. For a hot spot located beneath the northwestern Kerguelen plateau, or a hot spot located beneath Kerguelen with fixed source, very little overall motion during the past 100 Myr is predicted.

[65] Louisville: Some results are shown in Figure 16. For assumed plume age 121 Ma and the more northerly location (Table 1), they are similar to previous results. For a present-day hot spot position further southwest, as suggested by the hot spotting technique [*Wessel and Kroenke*, 1997], predicted past hot spot location is also further southwest. Since the link between Louisville hot spot and Ontong Java Plateau is rather uncertain, results for a younger

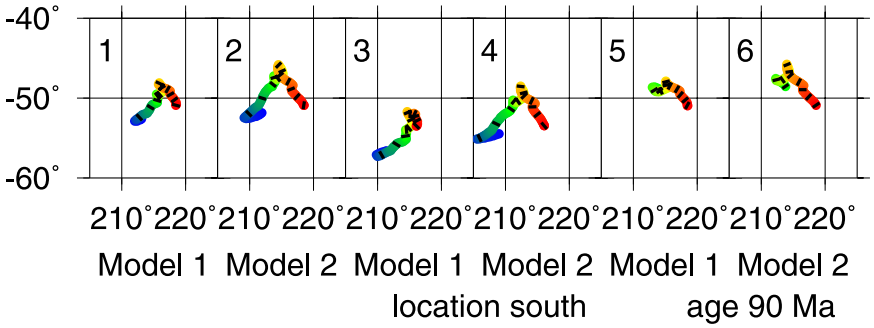

Figure 16. Computed Louisville hot spot motion. Assumed present location at 138.1°W, 50.9°S for panels 1, 2, 5, and 6 and at 141.2°W, 53.5°S for panels 3 and 4. Assumed hot spot age 121 Ma (panels 1–4) or 90 Ma (panels 5 and 6). Ambient mantle viscosity model 1 (panels 1, 3, 5) or 2 (panels 2, 4, 6). Results are identical for fixed and moving plume source. Color scale is the same as in Figure 11.

assumed hot spot age 90 Ma are also shown. These are, over the past 90 Myr, similar to the results for older age, and similar to previous results [*Koppers et al.*, 2004]. For a moving plume source, predicted hot spot motion tends to get less southward/more northward for higher buoyant rising speed (compare Figure 12 and Figure 11), representing flow deeper in the mantle.

[66] Marion: Previous results indicated a southward motion over the past 83 Myr. Whereas *O'Neill et al.* [2003] found a rather large drift of around 5–10°, the motion computed by *Steinberger* [2000] is less. Results obtained here are more similar to those of *Steinberger* [2000] with even less southward motion. A small hot spot motion is supported by paleomagnetic results [*Torsvik et al.*, 1998].

[67] Samoa: We assume here the same age (40 Ma) as *Hart et al.* [2004], larger than in earlier work, and we compute hot spot motion similar to the case shown by *Hart et al.* [2004].

[68] Tristan: Previous results indicated either motion in a southeasterly to southwesterly direction or an almost stationary hot spot. Here we compute motion in an east-southeasterly direction reflecting flow direction at greater depth in the mantle. However, motion is very slow (less than 1 cm/yr) in either case, so differences in predicted past hot spot locations are small. Again, this motion gets larger for higher assumed buoyant rising speed (compare Figure 12 and Figure 11).

5. Discussion

5.1. Temperature Anomalies

[69] Comparison of the temperature anomaly curves with observations places an approximate lower limit on the mass flux of plumes that can rise from the core-mantle boundary [*Albers and Christensen*, 1996]. There is a tradeoff between the inferred lower limit for B_0 of plumes that may arise from the lowermost mantle and the thermal diffusivity, which is uncertain within a factor of about two. If some plumes with about $B_0 = 10^3$ kg/s come from the lowermost mantle, average thermal diffusivity cannot be much larger than assumed here. For Iceland ($B_0 = 10^3$ kg/s) we compute a transition zone temperature anomaly 150 to 200 K, similar to what *Shen et al.* [1998, 2002] found. For a basal temperature anomaly of 500 K, we compute 250 K for Tahiti ($B_0 = 2 \cdot 10^3$ kg/s), slightly more than what *Niu et al.* [2002] found, and 300 K for Hawaii ($B_0 = 3 \cdot 10^3$ kg/s) in agreement with *Li et al.* [2000]. Thus our model temperature anomalies appear realistic, in particular for the lower basal temperature anomaly 500 K. Larger temperature drop for given mass flux, hence better agreement of the predictions for the higher basal temperature anomaly 750 K with observations would result with larger thermal diffusivities. However, much larger thermal diffusivity would increase the lower limit for buoyancy flux of plumes from the lower mantle to $>10^3$ kg/s hence we favor a lower basal temperature anomaly of about 500 K. In this case, resulting sublithospheric temperature anomalies between about 140 K (Iceland) and 260 K (Hawaii) are in agreement with a number of observational constraints [*Schubert et al.*, 2001; *Ruedas et al.*, 2004; *Putirka*, 2005]. For thermal plumes, temperature anomalies can be converted to density anomalies, but those would be smaller for thermochemical plumes, which could exhibit a great variety of plume shapes and sizes [*Farnetani and Samuel*, 2005].

[70] The left panel of Figure 5 shows seismic v_s anomaly inferred from the temperature anomaly. For Iceland with $B_0 \approx 10^3$ kg/s the expected anomaly is between 2 and 2.5% below the lithosphere and drops to about 1.5% in the transition zone, a trend that agrees with the seismic model of *Hung et al.* [2004], although their model yields somewhat larger anomalies. The anomaly strength should again increase in the upper part of the lower mantle, but a plume cannot be resolved there with current seismic models. *Hung et al.* [2004] point out that "if a plume-like low-velocity structure is present in the uppermost lower mantle beneath Iceland, it can be revealed unequivocally only by a network of ocean bottom seismic stations off Iceland." In the lower mantle, we expect anomalies of about 2% for a basal temperature anomaly of 500 K. *Montelli et al.* [2004] found smaller anomalies; they may correspond to an average anomaly lower than the centerline anomaly, due to limited resolution. The v_s anomalies obtained here are, especially for large plumes, somewhat higher than those in the models of *Goes et al.* [2004]. Differences come from the different starting plume temperature anomaly, and the conversion from temperature to seismic velocities: The conversion factors used here [*Steinberger and Calderwood*, 2006] are somewhat larger than those of *Goes et al.* [2004].

5.2. Plume Conduit Radius

[71] For ambient mantle viscosity profile 1, computed plume conduit radius in the upper mantle is in approximate agreement with seismological [*Hung et al.*, 2004; *Allen and Tromp*, 2005] and magnetotelluric [*Constable and Heinson*, 2004] results, but seismological images yield no evidence for such variations in radius as computed for viscosity profile 2. Also, for viscosity model 1 the computed plume radius in the transition zone is closer to the value of *Niu et al.* [2002]. Plume conduit radii in the lower mantle are mostly within the range observed by *Montelli et al.* [2004] and computed by *Goes et al.* [2004].

[72] In contrast to our results, *Goes et al.* [2004] find plumes to be substantially narrower above 660 km than below. This is in part due to their stronger viscosity contrast (our model has a more gradual viscosity increase with depth and a smaller jump across 660 km) and in part, because their power law exponent is the same above and below. At present, it is still a matter of debate, which creep mechanism (diffusion or dislocation) dominates where, and hence which power law exponent is appropriate.

5.3. Hot Spot Motion and Shape of Plume Conduits

[73] The largest difference from previous results occurs for the Kerguelen hot spot. Previous models tended to predict Kerguelen hot spot motion in southeasterly direction and thus allowed a better fit to geometry and ages of the Ninetyeast ridge and to paleolatitudes than the fixed hot spot model. A hot spot located beneath the northwestern Kerguelen plateau had been previously invoked to explain the geometry of the Ninetyeast ridge assuming hot spot fixity. Given that we compute an almost fixed hot spot for this location, this explanation remains valid. However, there is little observational support for such a present-day hot spot location: Given present-day volcanic activity, Heard Island (about 1000 km further southeast) seems a much more likely location, but this location is not suitable for fitting Ninetyeast Ridge with a fixed hot spot. Taking our new models of hot spot motion into account, the fit becomes even worse. The situation is similar with respect to paleomagnetic results: These tend to indicate latitudes further north than Kerguelen Island, as summarized by *Antretter et al.* [2002]. The misfit between computations and observations is kept relatively small for an assumed hot spot location beneath the northwestern Kerguelen plateau but becomes very large for a hot spot presently at Heard Island. It becomes even worse if true polar wander [*Besse and Courtillot*, 2002] is also considered. However note that the true polar wander curve of *Besse and Courtillot* [2002] was obtained under the assumption of fixed hot spots. A consistent treatment that takes hot spot motion into account, thus yielding a polar wander curve in the same mantle reference frame in which hot spot motion is computed, is currently under way (T. H. Torsvik et al., Global plate motion frames: Toward a unified model, submitted to *Earth-Science Reviews*, 2006). It thus remains unclear whether the Ninetyeast ridge is a proper "hot spot track" that formed right above the plume, or was formed by plume material flowing beneath the lithosphere and feeding into a leaky transform fault or fracture zone. The ocean floor age grid of *Müller et al.* [1997] in fact indicates that the Ninetyeast ridge runs along a fracture zone. In previous work, the largest variation of predicted hot spot motion was caused by which tomography model was used to infer mantle density anomalies, and hence large-scale mantle flow. It is therefore possible that in the

future improved flow models will again lead to a better fit between model and observations also for the Kerguelen hot spot.

[74] For other hot spots, results obtained here remain similar to previous results, hence we will not further discuss them, as resulting hot spot motion and shape of plume conduit has been extensively compared with observational constraints in previous work.

6. Conclusions and Perspectives for Future Work

[75] We have used here the results of *Albers and Christensen* [1996] to derive profiles of plume temperature anomalies versus depth. Our results are in agreement with a number of observations, in particular, if a temperature anomaly of only 500 K at the base of the plume in the lowermost mantle is assumed.

[76] Depth-dependent plume and ambient mantle viscosities are inferred and given these we computed thermal plume radius following *Schubert et al.* [2001]. For basal temperature anomaly 500 K, we find typical plume radii 150–200 km in the lower mantle, decreasing to about 100 km in the upper mantle. Again these numbers are approximately in accord with observations. Plume conduit radii, temperature anomalies and viscosity are used to compute conduit buoyant rising speeds. These were combined with large-scale mantle flow models to compute the shape of plume conduits and the motion of hot spots. A substantial viscosity decrease beneath the lithosphere was found necessary to prevent fast plate motions from tilting plume conduits too strongly. For a factor 1000 decrease in a 27 km thick layer, computed tilts in the upper mantle were found to be approximately in accord with observations. In this case, computed conduit shapes and hot spot motions were found to be mostly similar to previous results: Differences were mostly within the range of the large variations of results due to the uncertainties of other modeling parameters. Only for the Kerguelen hot spot the new results are substantially different: Whereas previously mostly a south- to southeastward motion had been found [*Antretter et al.*, 2002; *O'Neill et al.*, 2003, 2005] which helped to explain paleolatitudes and geometry of the Ninetyeast ridge, the new results do not help in reducing any misfit.

[77] Many of the assumptions that went into the computation of buoyant rising speed are considerably uncertain, and it may hence be necessary in the future to revise results presented here: An adiabatic temperature gradient was assumed in the mantle away from the top and bottom thermal boundary layers, however some numerical models yield a subadiabatic gradient [*Zhong*, 2006; *Bunge*, 2005]. Anomalous mass flux estimates adopted here are based on plume swells, but higher estimates are obtained from both seismic tomography [*Nolet et al.*, 2006] and dynamic models for thermal plumes [*Goes et al.*, 2004]. Effective activation enthalpy is uncertain because of uncertainties about how different creep mechanisms contribute to deformation at different depths, and it has even been suggested to be negative [*Korenaga*, 2005a]. Comparison with tomographic images [*Montelli et al.*, 2004] will be important to assess assumptions about plume source motion. On the positive side, predicted conduit thermal halo radius and buoyant rising speed are not very sensitive to the viscosity contrast inside and outside the plume, and the predicted hot spot motion is not very sensitive to buoyant rising speed either.

[78] Preliminary results [*Tan et al.*, 2006] show that it is possible to compute the motion and tilting of a plume in large-scale flow fully dynamically. For example, the influence of a fast-moving plate on plume conduit tilt can be studied with a fully dynamic model, whereas we had to introduce here a somewhat ad-hoc low-viscosity asthenosphere layer in order to match predicted plume conduit shape with observations. This approach is computationally expensive and therefore restricted to selected individual model runs. The approach taken here however has the advantage of being computationally very efficient: For each plume size we only do one instantaneous flow computation at high ($l = 255$) resolution to compute buoyant rising speed of the plume conduit. The time-dependent computation of large-scale flow and advection of plumes is done with a low-resolution flow field. Calibrating our simplified, computationally less demanding approach with fully dynamic computations can help to extend results of the latter to a much larger range of models.

Acknowledgments

[79] This research was motivated by suggestions from Geoff Davies and Ulrich Christensen. We also appreciate discussions with Ross Kerr, Saskia Goes, and Cinzia Farnetani and manuscript comments by Geoff Davies and Peter van Keken.

It was partially funded under DFG (ODP Germany) projects So72/63-2 and -3. Figures were prepared using GMT [*Wessel and Smith*, 1998].

References

Albers, M., and U. R. Christensen (1996), The excess temperature of plumes rising from the core-mantle boundary, *Geophys. Res. Lett.*, *23*, 3567–3570.

Albers, M., and U. R. Christensen (2001), Channeling of plume flow beneath mid-ocean ridges, *Earth Planet. Sci. Lett.*, *187*, 207–220.

Allen, R. M., and J. Tromp (2005), Resolution of regional seismic models: Squeezing the Iceland anomaly, *Geophys. J. Int.*, *161*, 373–386.

Allen, R. M., et al. (2002), Plume-driven plumbing and crustal formation in Iceland, *J. Geophys. Res.*, *107*(B8), 2163, doi:10.1029/2001JB000584.

Antretter, M., B. Steinberger, F. Heider, and H. Soffel (2002), Paleolatitudes of the Kerguelen hotspot: New paleomagnetic results and dynamic modeling, *Earth Planet. Sci. Lett.*, *203*, 635–650.

Antretter, M., P. Riisager, S. Hall, X. Zhao, and B. Steinberger (2004), Modeled paleolatitudes for the Louisville hotspot and the Ontong Java Plateau, in *Origin and Evolution of the Ontong Java Plateau*, edited by G. Fitton et al., *Geol. Soc. Spec. Publ.*, *229*, 21–30.

Becker, T., and L. Boschi (2002), A comparison of tomographic and geodynamic mantle models, *Geochem. Geophys. Geosyst.*, *3*(1), 1003, doi:10.1029/2001GC000168.

Besse, J., and V. Courtillot (2002), Apparent and true polar wander and the geometry of the geomagnetic field over the last 200 Myr, *J. Geophys. Res.*, *107*(B11), 2300, doi:10.1029/2000JB000050.

Boehler, R. (1996), Melting temperature of the Earth's mantle and core: Earth's thermal structure, *Annu. Rev. Earth Planet. Sci.*, *24*, 15–40.

Bunge, H.-P. (2005), Low plume excess temperature and high core heat flux inferred from non-adiabatic geotherms in internally heated mantle circulation models, *Phys. Earth Planet. Inter.*, *153*, 3–10.

Calderwood, A. R. (1999), Mineral physics constraints on the temperature and composition of the Earth's mantle, Ph.D. thesis, Univ. of Br. Columbia, Vancouver, B. C., Canada.

Chopelas, A., and R. Boehler (1989), Thermal expansion measurement at very high pressure, systematics, and a case for a chemically homogeneous mantle, *Geophys. Res. Lett.*, *16*, 1347–1350.

Christensen, U. R. (1983), Convection in a variable-viscosity fluid: Newtonian versus power-law rheology, *Earth Planet. Sci. Lett.*, *64*, 153–162.

Coffin, M. F., M. S. Pringle, R. A. Duncan, T. P. Gladczenko, M. Storey, R. D. Mueller, and L. A. Gahagan (2002), Kerguelen hotspot magma output since 130 Ma, *J. Petrol.*, *43*(7), 1121–1139.

Constable, S., and G. Heinson (2004), Hawaiian hot-spot swell structure from seafloor MT sounding, *Tectonophysics*, *389*, 111–124.

Courtillot, V., A. Davaille, J. Besse, and J. Stock (2003), Three distinct types of hotspots in the Earth's mantle, *Earth Planet. Sci. Lett.*, *205*, 295–308.

Davaille, A., F. Girard, and M. Le Bars (2002), How to anchor hotspots in a convecting mantle?, *Earth Planet. Sci. Lett.*, *203*, 621–634.

Davies, G. F. (1988), Ocean bathymetry and mantle convection: 1. Large-scale flow and hotspots, *J. Geophys. Res.*, *93*, 10,467–10,480.

Duncan, R. A., and D. A. Clague (1985), Pacific plate motion recorded by linear volcanic chains, in *The Ocean Basins and Margins*, vol. 7a, edited by A. E. M. Nairn, F. G. Stehli, and S. Uyeda, pp. 89–121, Springer, New York.

Duncan, R. A., P. R. Hooper, J. Rehacek, J. S. Marsh, and A. R. Duncan (1997), The timing and duration of the Karoo igneous event, southern Gondwana, *J. Geophys. Res.*, *102*, 18,127–18,138.

Dziewonski, A. M., and D. L. Anderson (1981), Preliminary Reference Earth Model, *Phys. Earth Planet. Inter.*, *25*, 297–356.

Farnetani, C. G. (1997), Excess temperature of mantle plumes: The role of chemical stratification across D″, *Geophys. Res. Lett.*, *24*, 1583–1586.

Farnetani, C. G., and H. Samuel (2005), Beyond the thermal plume paradigm, *Geophys. Res. Lett.*, *32*, L07311, doi:10.1029/2005GL022360.

Fitton, J. G., J. J. Mahoney, P. J. Wallace, and A. D. Saunders (2004), Leg 192 synthesis: Origin and evolution of the Ontong Java Plateau, in *Proceedings of the Ocean Drill. Program, Sci. Results* [online], vol. 192, edited by J. G. Fitton et al. (Available at http://www-odp.tamu.edu/publications/192_SR/synth/synth.htm)

Gilbert, L. A., and K. A. Foland (1986), The Mont St. Hilaire plutonic complex: Occurrence of excess ^{40}Ar and short intrusion history, *Can. J. Earth Sci.*, *23*, 948–958.

Goes, S., F. Cammarano, and U. Hansen (2004), Synthetic seismic signature of thermal mantle plumes, *Earth Planet. Sci. Lett.*, *218*, 403–419.

Hager, B. H., and R. J. O'Connell (1979), Kinematic models of large-scale mantle flow, *J. Geophys. Res.*, *84*, 1031–1048.

Hager, B. H., and R. J. O'Connell (1981), A simple global model of plate dynamics and mantle convection, *J. Geophys. Res.*, *86*, 4843–4867.

Hart, S. R., et al. (2000), Vailulu'u undersea volcano: The New Samoa, *Geochem. Geophys. Geosyst.*, *1*(12), doi:10.1029/2000GC000108.

Hart, S. R., M. Coetzee, R. K. Workman, J. Blusztajn, K. T. M. Johnson, J. M. Sinton, B. Steinberger, and J. W. Hawkins (2004), Genesis of the Western Samoa Seamount Province: Age, geochemical fingerprint and tectonics, *Earth Planet. Sci. Lett.*, *227*, 37–56, doi:10.1016/j.epsl.2004.08.005.

Hofmann, C., G. Féraud, and V. Courtillot (2000), ^{40}Ar/^{39}Ar dating of mineral separates and whole rocks from the Western Ghats lava pile: Further constraints on the duration and age of the Deccan Traps, *Earth Planet. Sci. Lett.*, *180*, 13–27.

Hung, S.-H., Y. Shen, and L.-Y. Chiao (2004), Imaging seismic velocity structure beneath the Iceland hot spot: A finite frequency approach, *J. Geophys. Res.*, *109*, B08305, doi:10.1029/2003JB002889.

Ingle, S., and M. F. Coffin (2004), Impact origin for the greater Ontong Java Plateau?, *Earth Planet. Sci. Lett.*, *218*, 123–134.

Jellinek, A. M., and M. Manga (2002), The influence of a chemical boundary layer on the fixity, spacing and lifetime of mantle plumes, *Nature*, *418*, 760–763.

Karato, S. (1993), Importance of anelasticity in the interpretation of seismic tomography, *Geophys. Res. Lett.*, *20*, 1623–1626.

Karato, S., S. Zhang, and H. R. Wenk (1995), Superplasticity in Earth's lower mantle: Evidence from seismic anisotropy and rock physics, *Science*, *270*, 458–461.

Kerr, R. C., and C. Mériaux (2004), Structure and dynamics of sheared mantle plumes, *Geochem. Geophys. Geosyst.*, *5*, Q12009, doi:10.1029/2004GC000749.

Korenaga, J. (2005a), Firm mantle plumes and the nature of the core-mantle boundary region, *Earth Planet. Sci. Lett.*, *232*, 29–37.

Korenaga, J. (2005b), Why did not the Ontong Java Plateau form subaerially?, *Earth. Planet. Sci. Lett.*, *234*, 385–399.

Koppers, A. A. P., R. A. Duncan, and B. Steinberger (2004), Implications of a nonlinear $^{40}Ar/^{39}Ar$ age progression along the Louisville seamount trail for models of fixed and moving hot spots, *Geochem. Geophys. Geosyst.*, *5*, Q06L02, doi:10.1029/2003GC000671.

Li, X., R. Kind, K. Priestley, S. V. Sobolev, F. Tilmann, X. Yuan, and M. Weber (2000), Mapping the Hawaiian plume conduit with converted seismic waves, *Nature*, *405*, 938–941.

McNamara, A. K., and S. Zhong (2004), The influence of thermochemical convection on the fixity of mantle plumes, *Earth Planet. Sci. Lett.*, *222*, 485–500.

Montelli, R., G. Nolet, F. A. Dahlen, G. Masters, E. R. Engdahl, and S.-H. Hung (2004), Finite-frequency tomography reveals a variety of plumes in the mantle, *Science*, *303*, 338–343.

Morgan, W. J. (1972), Deep mantle convection plumes and plate motions, *Am. Assoc. Pet. Geol. Bull.*, *56*, 203–213.

Müller, R. D., W. R. Roest, J.-Y. Royer, L. M. Gahagan, and J. G. Sclater (1997), Digital isochrons of the world's ocean floor, *J. Geophys. Res.*, *102*, 3211–3214.

Niu, F., S. C. Solomon, P. G. Silver, D. Suetsugu, and H. Inoue (2002), Mantle transition-zone structure beneath the South Pacific Superswell and evidence for a mantle plume underlying the Society hotspot, *Earth Planet. Sci. Lett.*, *198*, 371–380.

Nolet, G., S.-I. Karato, and R. Montelli (2006), Plume fluxes from seismic tomography, *Earth. Planet. Sci. Lett.*, *248*, 685–699.

O'Connor, J. M., and A. P. le Roex (1992), South Atlantic hot spot-plume systems: 1. Distribution of volcanism in time and space, *Earth Planet. Sci. Lett.*, *113*, 343–364.

Olson, P., G. Schubert, and C. Anderson (1993), Structure of axisymmetric mantle plumes, *J. Geophys. Res.*, *98*, 6829–6844.

O'Neill, C., D. Müller, and B. Steinberger (2003), Geodynamic implications of moving Indian Ocean hotspots, *Earth Planet. Sci. Lett.*, *215*, 151–168, doi:10.1016/S0012-821X(03)00368-6.

O'Neill, C., D. Müller, and B. Steinberger (2005), On the uncertainties in hot spot reconstructions and the significance of moving hot spot reference frames, *Geochem. Geophys. Geosyst.*, *6*, Q04003, doi:10.1029/2004GC000784.

Putirka, K. D. (2005), Mantle potential temperatures at Hawaii, Iceland, and the mid-ocean ridge system, as inferred from olivine phenocrysts: Evidence for thermally driven mantle plumes, *Geochem. Geophys. Geosyst.*, *6*, Q05L08, doi:10.1029/2005GC000915.

Ranalli, G. (1995), *Rheology of the Earth*, 2nd ed., CRC Press, Boca Raton, Fla.

Renne, P. R., J. M. Glen, and S. C. Milner (1996), Age of Etendeka flood volcanism and associated intrusions in southwestern Africa, *Geology*, *24*, 659–662.

Ribe, N. M., and U. R. Christensen (1999), The dynamical origin of Hawaiian volcanism, *Earth Planet. Sci. Lett.*, *171*, 517–531.

Richards, M. A., and R. W. Griffiths (1988), Deflection of plumes by mantle shear flow: Experimental results and a simple theory, *Geophys. J.*, *94*, 367–376.

Ruedas, T., H. Schmeling, G. Marquart, A. Kreutzmann, and A. Junge (2004), Temperature and melting of a ridge-centred plume with application to Iceland. Part I: Dynamics and crust production, *Geophys. J. Int.*, *158*, 729–743.

Schilling, J.-G. (1991), Fluxes and excess temperatures of mantle plumes inferred from their interaction with migrating mid-ocean ridges, *Nature*, *352*, 397–403.

Schubert, G., and R. N. Hey (1986), Mantle viscosity beneath the Galapagos 95.5°W propagating rift, *Geophys. Res. Lett.*, *13*, 329–332.

Schubert, G., D. L. Turcotte, and P. Olson (2001), *Mantle Convection in the Earth and Planets*, Cambridge Univ. Press, New York.

Shen, Y., S. C. Solomon, I. T. Bjarnason, and C. J. Wolfe (1998), Seismic evidence for a lower mantle origin of the Iceland mantle plume, *Nature*, *395*, 62–65.

Shen, Y., et al. (2002), Seismic evidence for a tilted mantle plume and north-south mantle flow beneath Iceland, *Earth Planet. Sci. Lett.*, *197*, 261–272.

Sleep, N. (1990), Hotspots and mantle plumes: Some phenomenology, *J. Geophys. Res.*, *95*, 6715–6736.

Stacey, F. D. (1992), *Physics of the Earth*, 3rd ed., John Wiley, Hoboken, N. J.

Steinberger, B. (2000), Plumes in a convecting mantle: Models and observations for individual hotspots, *J. Geophys. Res.*, *105*, 11,127–11,152.

Steinberger, B. (2002), Motion of the Easter hot spot relative to Hawaii and Louisville hot spots, *Geochem. Geophys. Geosyst.*, *3*(11), 8503, doi:10.1029/2002GC000334.

Steinberger, B., and A. R. Calderwood (2006), Models of large-scale viscous flow in the Earth's mantle with constraints from mineral physics and surface observations, *Geophys. J. Int.*, doi:10.1111/j.1365-246X.2006.03131.x, in press.

Steinberger, B., and R. J. O'Connell (1998), Advection of plumes in mantle flow: Implications for hotspot motion, mantle viscosity and plume distribution, *Geophys. J. Int.*, *132*, 412–434.

Steinberger, B., and R. J. O'Connell (2000), Effects of mantle flow on hotspot motion, in *The History and Dynamics of Global Plate Motions*, *Geophys. Monogr. Ser.*, vol. 121, edited by M. A. Richards, R. G. Gordon, and R. D. van der Hilst, pp. 377–398, AGU, Washington, D. C.

Steinberger, B., R. Sutherland, and R. J. O'Connell (2004), Prediction of Emperor-Hawaii seamount locations from a revised model of global plate motion and mantle flow, *Nature*, *430*, 167–173, doi:10.1038/nature02660.

Tan, E., E. Choi, P. Thoutireddy, M. Gurnis, and M. Aivazis (2006), GeoFramework: Coupling multiple models of mantle convection within a computational framework, *Geochem. Geophys. Geosyst.*, *7*, Q06001, doi:10.1029/2005GC001155.

Tarduno, J. A., et al. (2003), The Emperor Seamounts: Southward motion of the Hawaiian hotspot plume in Earth's mantle, *Science*, *301*, 1064–1069.

Torsvik, T. H., R. D. Tucker, L. D. Ashwal, E. A. Eide, N. A. Rakotosolofo, and M. J. De Wit (1998), Late Cretaceous magmatism in Madagascar: Palaeomagnetic evidence for a stationary Marion hotspot, *Earth Planet Sci. Lett.*, *164*, 221–232.

Wang, Z. W. (1999), The melting of Al-bearing perovskite at the core-mantle boundary, *Phys. Earth Planet. Inter.*, *115*, 219–228.

Weertman, J., and J. R. Weertman (1975), High temperature creep of rock and mantle viscosity, *Annu. Rev. Earth Planet. Sci.*, *3*, 293–315.

Weis, D., F. A. Frey, R. Schlich, M. Schaming, R. Montigny, D. Damasceno, N. Mattielli, K. E. Nicolaysen, and J. S. Scoates (2002), Trace of the Kerguelen mantle plume: Evidence from seamounts between the Kerguelen Archipelago and Heard Island, Indian Ocean, *Geochem. Geophys. Geosyst.*, *3*(6), 1033, doi:10.1029/2001GC000251.

Wessel, P., and L. W. Kroenke (1997), A geometric technique for relocating hotspots and refining absolute plate motions, *Nature*, *387*, 365–369.

Wessel, P., and W. H. F. Smith (1998), New, improved version of the Generic Mapping Tools released, *Eos Trans. AGU*, *79*, 579.

Wölbern, I., A. W. B. Jacob, T. A. Blake, R. Kind, X. Li, X. Yuan, F. Duennebier, and M. Weber (2006), Deep origin of the Hawaiian tilted plume conduit derived from receiver functions, *Geophys. J. Int.*, *166*, 767–781.

Xu, Y., T. J. Shankland, S. Linhardt, D. C. Rubie, F. Langenhorst, and K. Klasinski (2004), Thermal diffusivity and conductivity of olivine, wadsleyite and ringwoodite to 20 GPa and 1373 K, *Phys. Earth Planet. Inter.*, *143–144*, 321–336.

Yamazaki, D., and S.-I. Karato (2001), Some mineral physics constraints on the rheology and geothermal structure of Earth's lower mantle, *Am. Mineral.*, *86*, 385–391.

Zerr, A., and R. Boehler (1994), Constraints on the melting temperature of the lower mantle from high-pressure experiments on MgO and magnesiowüstite, *Nature*, *371*, 506–508.

Zhong, S. (2006), Constraints on thermochemical convection of the mantle from plume heat flux, plume excess temperature, and upper mantle temperature, *J. Geophys. Res.*, *111*, B04409, doi:10.1029/2005JB003972.

Zhong, S., M. T. Zuber, L. Moresi, and M. Gurnis (2000), Role of temperature-dependent viscosity and surface plates in spherical shell models of mantle convection, *J. Geophys. Res.*, *105*, 11,063–11,082.